Materials Today Bio 32 (2025) 101676

Contents lists available at ScienceDirect

Materials Today Bio

journal homepage: www.journals.elsevier.com/materials-today-bio

Hyaluronic acid-based hydrogel microspheres with multi-responsive properties for antibacterial therapy and bone regeneration in *Staphylococcus aureus*-infected skull defects

Xiaolong Lin [a,1], Shuli Deng [a,1], Tao Fu [b,1], Yuqing Lei [c,1], Ying Wang [a], Jiapei Yao [d], Yaojun Lu [d], Yong Huang [d], Jingjing Shang [e], Jingjing Chen [d,f,*], Xindie Zhou [d,g,**]

[a] *Stomatology Hospital, School of Stomatology, Zhejiang University School of Medicine, Zhejiang Provincial Clinical Research Center for Oral Diseases, Key Laboratory of Oral Biomedical Research of Zhejiang Province, Cancer Center of Zhejiang University, Engineering Research Center of Oral Biomaterials and Devices of Zhejiang Province, Hangzhou, 310000, China*

[b] *Department of Oral and Maxillofacial Surgery, The Second Affiliated Hospital of Zhejiang University School of Medicine, School of Stomatology and Key Laboratory of Oral Biomedical Research of Zhejiang Province, Hangzhou, Zhejiang, 310000, China*

[c] *Department of Minimally Invasive Interventional Radiology, The Second Affiliated Hospital, School of Biomedical Engineering Guangzhou Medical University, Guangzhou, Guangdong, 510260, China*

[d] *Department of Orthopedics, The Second People's Hospital of Changzhou, The Third Affiliated Hospital of Nanjing Medical University, Changzhou Medical Center, Changzhou, 213000, China*

[e] *Department of Pharmacy, The Second People's Hospital of Changzhou, The Third Affiliated Hospital of Nanjing Medical University, Changzhou Medical Center, Changzhou, Jiangsu, 213000, China*

[f] *Department of Immunology, Key Laboratory of Immune Microenvironment and Diseases, NHC Key Laboratory of Antibody Technique, Jiangsu Key Lab of Cancer Biomarkers, Prevention and Treatment, Collaborative Innovation Center for Personalized Cancer Medicine, Nanjing Medical University, Nanjing, China*

[g] *Department of Orthopedics, Gonghe County Hospital of Traditional Chinese Medicine, Hainan Tibetan Autonomous Prefecture, Qinghai Province, 811800, China*

ARTICLE INFO

Keywords:
Antimicrobial peptides
Microspheres
Hyaluronic acid
Bone defect
Immune microenvironment

ABSTRACT

This study introduces hyaluronic acid-based (HA) hydrogel microspheres loaded with zinc oxide nanoparticles (ZnO-NPs) for the treatment of infectious bone defects. The microspheres were fabricated using a 3D-printing process, with a formulation consisting of 6 wt% HAD (methacrylated HA), 3 wt% AOHA (AMP-conjugated oxidized HA), 1 % BOHA (phenylboric acid-conjugated HA), 0.5 % photoinitiator, and 0.05 % ZnO-NPs. *In vitro*, the hydrogel microspheres demonstrated significant antibacterial activity against *Staphylococcus aureus*, with colony counts and biofilm inhibition assays showing a marked reduction in bacterial growth after 12 and 24 h. The release of antimicrobial peptides (AMPs) was enhanced in acidic conditions and in the presence of hyaluronidase. The microspheres also promoted osteogenic differentiation of bone marrow stromal cells (BMSCs), as evidenced by increased expression of osteogenic markers (ALP, OCN, OPN, and COL-1). *In vivo*, the hydrogel microspheres were tested in a rat skull defect model, showing significant bone regeneration, improved angiogenesis, and an anti-inflammatory response. These results indicate that ABOHA@ZnO hydrogel microspheres provide a promising strategy for treating infectious bone defects by combining antimicrobial, osteogenic.

1. Introduction

The treatment of infectious bone defects has long been a challenge in orthopedics. Owing to the complexity of bone tissue and the multiple biological requirements for repair, traditional treatment methods such as antibiotic therapy and bone grafting often fail to achieve optimal therapeutic outcomes [1]. However, advancements in tissue engineering and biomaterials science have introduced hydrogel-based scaffolds as a

* Corresponding author. Department of Orthopedics, The Second People's Hospital of Changzhou, The Third Affiliated Hospital of Nanjing Medical University, Changzhou Medical Center, Changzhou, 213000, China.

** Corresponding author. Department of Orthopedics, The Second People's Hospital of Changzhou, The Third Affiliated Hospital of Nanjing Medical University, Changzhou Medical Center, Changzhou, 213000, China.

E-mail addresses: chenjingjing@njmu.edu.cn (J. Chen), zhouxindie@njmu.edu.cn (X. Zhou).

[1] These authors contributed equally to this work.

https://doi.org/10.1016/j.mtbio.2025.101676
Received 30 December 2024; Received in revised form 20 February 2025; Accepted 16 March 2025
Available online 26 March 2025

new strategy for bone defect treatment, thanks to their unique biocompatibility and tunable physical and chemical properties [2]. Hydrogels with intelligent response functions, which regulate drug release based on local microenvironmental changes (such as pH changes, enzyme activity, and reactive oxygen species (ROS) levels), have become a key area of research [3].

Hyaluronic acid (HA), a natural polysaccharide, has garnered significant attention due to its excellent biocompatibility, degradability, and broad application in tissue engineering [4]. HA-based hydrogels can mimic the three-dimensional network structure of the extracellular matrix, providing an optimal growth environment for cells [5]. However, the antimicrobial and antioxidant properties of HA hydrogels alone are limited. Therefore, hyaluronic acid-based hydrogels are designed to respond to various stimuli, such as pH, temperature, and enzymatic activity, which hold significant potential for the treatment of infectious bone defects [6,7]. To address this limitation, this study developed a novel 3D-printed HA microsphere hydrogel that integrates multiple response mechanisms and can intelligently respond to changes in the microenvironment of infected bone defects. MRSA (Methicillin-resistant *Staphylococcus aureus*) presents a significant challenge in the treatment of infectious bone defects due to its resistance to multiple antibiotics, which makes it difficult to eliminate the infection with conventional treatment methods [8]. Furthermore, the inflammatory response and tissue damage triggered by MRSA infection add to the complexity of repairing bone defects [9]. Consequently, treatment must not only intensify anti-infective strategies but also facilitate the simultaneous reconstruction of bone tissue. Antimicrobial peptides (AMPs) and their hydrogels offer many advantages in treating infectious diseases. AMPs are a crucial component of the natural immune defense system, exhibiting a broad spectrum of anti-infective activity. They can effectively target various bacteria, including gram-positive (G+) and gram-negative (G−) bacteria, as well as multidrug-resistant bacteria [10]. Additionally, AMPs are less prone to resistance than conventional antibiotics, have low toxicity, are biologically diverse, and can directly attack pathogens [6,11]. Zinc oxide nanoparticles (ZnO-NPs) have gained attention for their antibacterial activity and low toxicity, particularly in orthopedic implants. ZnO-NPs not only demonstrate effective antibacterial properties but also have the potential to promote osteogenesis [12]. The antibacterial mechanism of ZnO-NPs primarily involves the release of zinc ions, which inhibit bacterial growth [13]. In orthopedics, ZnO-NPs enhance osteogenic properties by promoting cell proliferation and osteogenic differentiation, improving the antibacterial and bone integration capabilities of orthopedic implants [14,15]. Moreover, ZnO-NPs have been used to support infectious bone regeneration. For instance, a composite scaffold with a bone-like structure was developed through the co-assembly of collagen fibers and ZnO nanowires, showing good antibacterial activity and promoting bone healing in both *in vitro* and *in vivo* studies [16]. By combining hyaluronic acid (HA), antimicrobial peptides (AMPs), and zinc oxide nanoparticles (ZnO-NPs), HA serves as a matrix material that provides support and promotes cell adhesion and proliferation; AMPs exert antimicrobial activity to effectively combat infections; ZnO-NPs not only possess antimicrobial properties but also promote osteogenesis and immune modulation. The synergistic interaction of these components enhances the hydrogel's overall efficacy in infection control, bone repair, and immune modulation, offering a multifunctional therapeutic strategy.

Significant progress has been made in the application of smart 3D-printed hydrogel microspheres in the field of bone defect healing [17,18]. These microspheres can responsively release drugs or growth factors in response to external stimuli such as pH changes, temperature, or biomolecule variations, promoting the regeneration of bone tissue. Researchers have successfully designed various smart hydrogel formulations with good biocompatibility and high mechanical strength, and can precisely control the shape and size of the microspheres through 3D printing technology to achieve personalized treatment [19,20]. In addition, these microspheres can also serve as cell carriers, improving the survival rate of cell transplantation and the integration effect of bone [21]. With the development of material science and bioprinting technology, smart 3D-printed hydrogel microspheres are expected to play a greater role in the treatment of bone defects. Ordinary hydrogels have been extensively studied for their application in bone defect repair [22], compared to traditional hydrogels, 3D-printed hydrogel microspheres offer more precise structural control and better biomechanical properties and can also effectively increase local drug concentrations, and with the degradation of the hydrogel [23]. The 3D-printed hyaluronic acid hydrogel has unique advantages over other 3D-printed hydrogel microspheres in bone defect repair. Its natural biocompatibility reduces immune rejection and promotes cell adhesion and proliferation. Hyaluronic acid can regulate multiple signaling pathways to accelerate osteogenic differentiation [24]. Compared to synthetic hydrogels it exhibits superior bone integration and bioactivity [25]. Therefore, this study used HA, AMPs, and ZnO NPs to construct multi-response 3D-printed hydrogel microspheres, offering a new approach for treating infectious bone defects.

Scheme 1a illustrates the synthesis procedure of ABOHA@ZnO hydrogel microspheres. The hydrogel system designed in this study can release AMPs through the breakage of chemical bonds caused by local pH reduction from bacterial activity or hyaluronidase produced by bacteria in bone defects, effectively inhibiting bacterial infection. Additionally, considering the production of ROS during infection, the hydrogels also incorporate ROS response mechanisms. When ROS levels increase in the body, hydrogels release phenylboric acid by breaking chemical bonds to eliminate excess ROS and reduce oxidative stress damage to cells (Scheme 1b). Additionally, ZnO NPs were incorporated into the hydrogel microspheres. In this study, the inclusion of ZnO NPs not only improved the hydrogel's antibacterial capabilities but also expedited bone defect repair by broad-spectrum bactericidal effects and activating multiple signaling pathways (Scheme 1c).

2. Materials and methods

2.1. Synthesis of HAD, OHA, AOHA, and BOHA hydrogel

An unsaturated double bond was grafted onto HA (200 kDa) to obtain HAD (Hyaluronic acid with unsaturated double bonds) by esterification with methacrylic anhydride and the hydroxyl groups in the HA side chain. HA was completely dissolved by stirring in ultrapure water at 2 (weight percentage) wt%, Dimethylformamide (DMF) was then added in drops to the solution (volume ratio water: DMF = 3:2) and stirred well, and the mixture was cooled to 4 °C. Methacrylic anhydride was added to the mixture in 3:1 amounts, and the reaction was maintained for 24 h. The polymer was precipitated by the addition of ethanol, and dialyzed in deionized water for 3 d. Purified HAD was recovered by freeze-drying for later use. The pH of deionized water was adjusted to 6.0 with dilute hydrochloric acid. HA was weighed and dissolved in deionized water at pH 6 to a 1 wt% concentration to ensure full dissolution. A 0.25 mol/L sodium periodate solution was added, and the mixture was magnetically stirred at 40 °C for 3 h. After adding 30 mL of glycol to terminate the reaction, the mixture was dialyzed against deionized water for 3 d and then lyophilized to obtain OHA (Oxidized hyaluronic acid). OHA was dissolved in deionized water (2 wt%), then GL13K AMPs (GKIIKLKASLKLL-NH_2, formula weight 1424 g/mol) were added. GL13K is a synthetic antimicrobial peptide (AMP) known for its broad-spectrum antimicrobial activity, particularly effective against both Gram-positive and Gram-negative bacteria. It exerts its antimicrobial effects by disrupting bacterial membranes, leading to cell membrane destabilization and subsequent bacterial death. In addition to its antimicrobial properties, GL13K has been shown to induce macrophage polarization towards the M2 phenotype, which plays a crucial role in modulating the immune response and promoting tissue repair and regeneration, making it beneficial for applications in infection control and wound healing. The solution was stirred at room

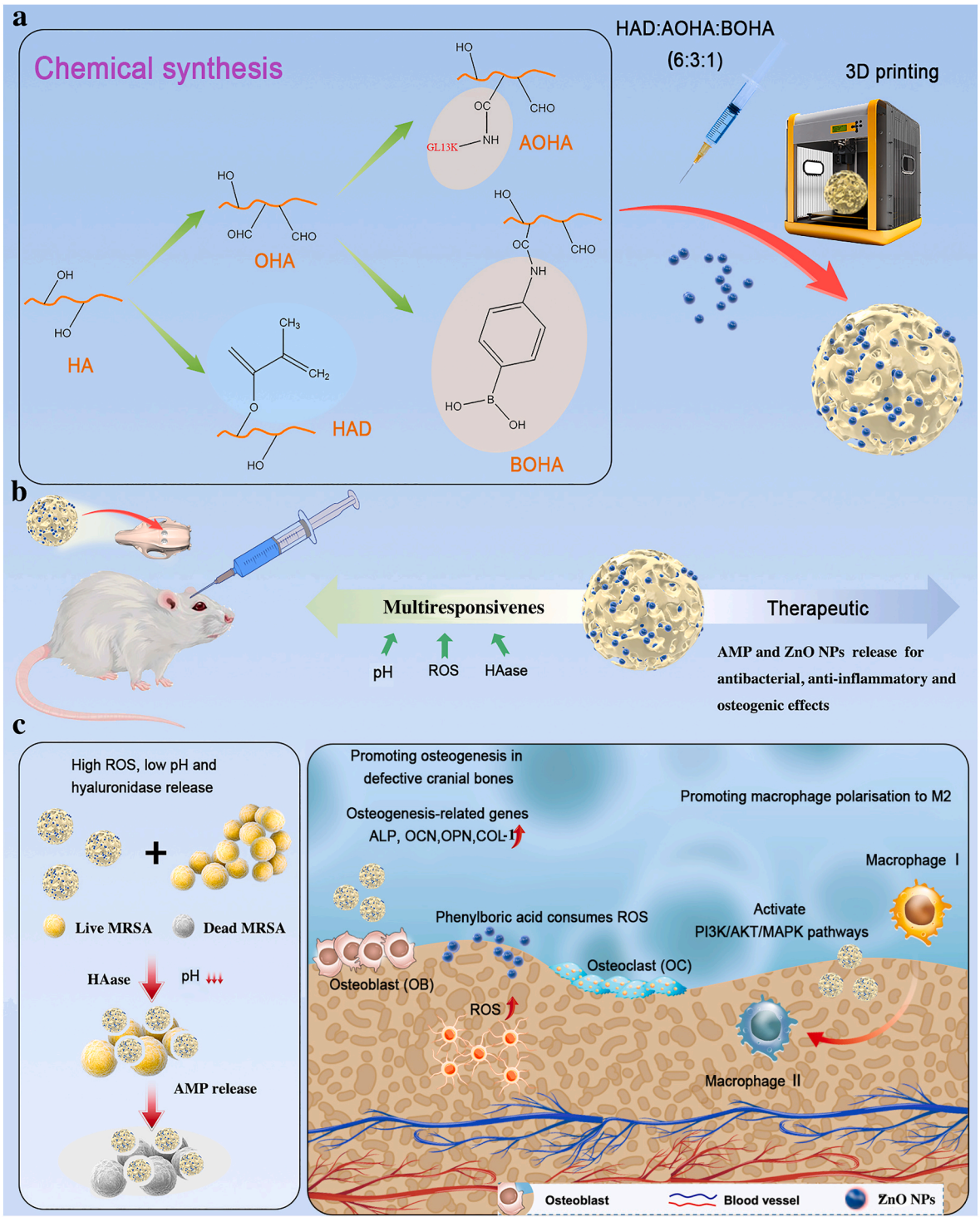

Scheme 1. Hyaluronic acid microspheres accelerate healing of infected bone defects process. (a) Synthesis procedure of ABOHA@ZnO hydrogel microspheres. (b)*In vivo* tests. and (c) Healing process after hydrogel microspheres treatment.

temperature for 12 h and dialyzed with deionized water for 48 h. Finally, AOHA (Antimicrobial peptide-Oxidized hyaluronic acid) was obtained by freeze-drying. Similarly, OHA was dissolved in deionized water (2 wt%), and 3-aminophenylboric acid (2 wt%) was added. The solution was stirred at room temperature for 12 h and dialyzed with deionized water for 48 h. Finally, BOHA (Phenylboric acid-Oxidized hyaluronic acid) was obtained by freeze-drying.

2.2. ABOHA @ ZnO hydrogel microsphere preparation

After filtering through a 0.22-μm membrane, the hydrogel mixture, enriched with ZnO-NPs (<30 nm particle size, >97 %, Aladdin Reagent, China, formula weight 81.39 g/mol), was prepared with the following composition: 6 wt% HAD, 3 wt% AOHA, 1 wt% BOHA, 0.5 wt% photoinitiator, and 0.05 wt% ZnO NPs, and the oil phase (a blend of 95 % weight paraffin and 5 % weight Span 80) was added to the ink tank of a computer-driven 3D printing machine (EFL-BP-6601, Yongqinquan

Intelligent Equipment Co., Ltd., Suzhou, China). Each 50-μm-thick layer was exposed to ultraviolet light (wavelength of 405 nm) for 15 s to polymerize into hydrogel microspheres. The resulting microspheres were then harvested, immersed in phosphate-buffered saline (PBS) for 12 h to remove any unpolymerized ink and carmine residues, with the PBS being replaced three times during this period.

2.3. Characterization of hydrogels microsphere

The chemical composition of the microsphere was characterized using Fourier transform infrared spectrophotometry (Bruker Vector 22, Bruker Optics, Germany). Each spectrum, recorded with 64 scans at a resolution of 4.0 cm^{-1}, was blended with a potassium bromide pellet. Proton nuclear magnetic resonance (^1H NMR) spectroscopy (Bruker AVANCE III 500, Germany; 40 °C in deuterated H_2O) was also used. The surface morphology of the hydrogel microspheres after freeze-drying was observed with field emission scanning electron microscopy (Nova Nano 450, Thermo FEI, Czech) at an accelerating voltage of 5 kV with platinum sputtering. Additionally, the growth of Bone marrow stromal cells (BMSCs) on the microspheres was assessed using confocal laser microscopy.

2.4. In vitro degradation test

To evaluate the breakdown of microgels, 100 mg portions of microspheres were added to 1 mL of PBS solution with 2 U/mL collagenase and agitated in a shaker at 37 °C and 120 rpm. Fresh supernatant was added daily to maintain enzymatic activity. The microgels were collected and rinsed with sterile, deionized water at set intervals. After freeze-drying, the weight of the microgels was measured, and the degradation percentage (D) was calculated using the formula: $D(\%) = (W_0 - W_t)/W_0 \times 100$ %, where W_0 is the initial weight and W_t is the weight at time t.

2.5. In vitro release profile under different environments

Samples were placed in a 50-mL centrifuge tube containing 10 mL of solutions in different environments adjusted with PBS and were incubated in a constant temperature shaker at 37 °C with 120 cycles/min. The released solution was collected on various time points, stored at −20 °C, and analyzed using an enzyme-linked immunosorbent assay kit. The cumulative release curve was plotted based on the initial content.

2.6. Antioxidant capacity of hydrogel microsphere

The study assessed the intracellular ROS scavenging capacity following hydrogel microsphere treatment using a ROS assay kit from Beyotime Biotechnology (Cat. No. S0033S, Shanghai, China). BMSCs were plated at 4×10^4 cells per well in 24-well plates, allowed to adhere for 24 h, and then exposed to a fluorescent probe (2′,7′-Dichlorodihydrofluorescein Diacetate, 1:1000 dilution) in a serum-free medium at 37 °C for 30 min. After washing, 100 μM H_2O_2 was added for co-culture with the hydrogel microspheres. Cells in serum-free medium served as the negative control, while those in a H_2O_2-containing medium without hydrogel served as the positive control. After 1 h, the medium was replaced, and cells were washed with PBS. ROS levels were assessed using bright-field and fluorescence microscopy, and 2′,7′-Dichlorodihydrofluorescein Diacetate stained cells were analyzed by flow cytometry for fluorescence intensity.

2.7. Biosafety assessment

BMSCs were selected as test cells and plated at 5×10^3 cells per well in 96-well plates. They were cultured in media with 0.5 % HAD hydrogel extract, 0.5 % AMP, and 0.5 % ABOHA@ZnO hydrogel microsphere extract, with PBS as the blank. The CCK-8 assay was used to assess cytotoxicity and proliferation at 24 and 48 h, in triplicate, followed by 2 h of incubation with CCK-8 at 37 °C. Absorbance was measured at 450 nm using a microplate reader. Cell compatibility was evaluated with the Live/Dead staining kit, with BMSCs seeded at 2×10^4 cells per well in 24-well plates under the same conditions as those for the CCK-8 assay. Live cells were stained with CA-AM (green) and dead cells with PI (red) at 24 and 48 h, in triplicate, and observed under a fluorescence microscope.

2.8. In vitro experiments

2.8.1. Antibacterial activity test and anti-biofilm effects

The antibacterial efficacy of ABOHA@ZnO hydrogel was evaluated by the colony count on plates. Methicillin-Resistant *Staphylococcus aureus* (MRSA) ATCC 3359 was first grown on columbia sheep blood agar under microaerophilic conditions at 37 °C for 24 h and then transferred into BHI at a concentration of 0.5 McFarland (MCF) (1.5×10^8 CFU/ml). The 100 μl MRSA suspensions were added in sterile tubes containing 5 ml BHI and 1 ml experimental solution (0.5 % HAD hydrogel extract, 0.5 % AMP and 0.5 % ABOHA@ZnO hydrogel microsphere extract), and the colony count were conducted after 12 and 24h culture under microaerophilic conditions at 37 °C.

In the context of anti-biofilm assessments, 100 μl of MRSA suspensions were placed into a sterile 48-well plate, which already contained either 200 μl of BHI broth or 200 μl of the experimental solution (comprising 0.5 % HAD hydrogel extract, 0.5 % AMP, and 0.5 % ABOHA@ZnO hydrogel microsphere extract) per well. The plates were then subjected to incubation under conditions of reduced oxygen at a temperature of 37 °C. The development of biofilms was assessed following 12 and 24 h of incubation, and the samples were prepared for analysis using previously established methods. Biofilm specimens were stained with Live/Dead BacLight Bacterial Viability Kit (Invitrogen, USA). Biofilms were observed under a laser confocal microscope (Zeiss LSM 710, Carl Zeiss, Germany). All the biofilm images were captured and saved using Zen 2010 Light Edition (Carl Zeiss, Germany). The biofilm integrated optical density (IOD) and Live/Dead ratio were evaluated by using ImageJ software.

2.9. In vitro osteogenic and angiogenesis ability of ABOHA @ ZnO hydrogel microspheres

2.9.1. Alkaline phosphatase (ALP)activity and alizarin red S (ARS) staining

The microspheres's ability to promote bone formation was assessed by evaluating calcium deposit formation and ALP activity. BMSCs were cultured at 37 °C with 5 % CO_2, as described in Section 2.6.1, and switched to an osteogenic medium at 60 % confluence (Cyagen, China). ALP activity and staining were conducted on day 14 using kits from Beyotime Biotech and Leagene Biotechnology, respectively, following the instructions. Calcium deposits were detected and quantified on day 14 using the ARS kit (Cyagen) and a microplate reader, with perchloric acid used for dissolution. Normalization involved adding cetylpyridinium chloride and sodium phosphate solutions to the samples, with absorbance read at 562 nm. Both the ALP activity assessment and the ARS quantification were conducted after treatment with the eluent from the microgel.

2.9.2. Immunofluorescence staining

Primary BMSCs were cultured on slides with medium containing leachate. After washing with 1 × PBS, cells were fixed in 4 % paraformaldehyde for 20 min at 25 °C. Following permeabilization with 0.1 % Triton X-100 and blocking with a blocking buffer, cells were incubated overnight at 4 °C with primary antibodies against osteopontin (OPN) and osteocalcin (OCN; Abcam). The next day, cells were washed and treated with Alexa Fluor® 594-conjugated secondary antibodies for 1 h at 25 °C. Nuclei were stained with DAPI, and the samples were

imaged using a confocal microscope.

2.9.3. Western blotting

For the western blot analysis, BMSCs and human umbilical vein endothelial cells (HUVECs) from four groups were cultured for 7 d before lysing with RIPA buffer for total protein extraction. Protein concentrations were determined using a bicinchoninic acid (BCA) assay kit (Thermo Fisher Scientific). Proteins were then denatured, resolved by SDS-PAGE, and transferred to polyvinylidene difluoride membranes. The membranes were probed overnight at 4 °C with primary antibodies against Runx2, OCN, OPN, and COL, and subsequently with horseradish peroxidase (HRP)–tagged secondary antibodies. Protein detection was performed using an enhanced chemiluminescent kit (Thermo Fisher Scientific), and band images were captured using Scion imaging software. Western blotting was also conducted to verify the activation of the PI3K-AKT and MAPK pathways by ABOHA@ZnO hydrogel microspheres. Cells were cultured in six-well plates at a density of 4×10^5 cells per well for 48 h. Protein extraction was followed by quantification using the BCA assay and separation through SDS-PAGE. After blocking with 5 % milk, membranes were incubated overnight at 4 °C with primary antibodies (AKT, p-AKT, PI3K, p-PI3K, MEK1/2, p-MEK1/2, ERK1/2, p-ERK1/2, and GAPDH; Abcam). Membranes were then washed and incubated with secondary antibodies for 1 h at room temperature. Protein bands were visualized and quantified through chemiluminescence.

2.9.4. Quantitative polymerase chain reaction

Quantitative polymerase chain reaction (qPCR) was used to assess the expression of osteogenic and angiogenesis markers: ALP, OCN, OPN, collagen I (COL I), platelet endothelial cell adhesion molecule-1 (CD31), and vascular endothelial growth factor (VEGF) after 7 d of cell incubation. Cellular total RNA was isolated with TRIzol reagent (Invitrogen, USA) and converted to complementary DNA (cDNA) using a PrimeScript RT kit (Takara, Japan). Real-time PCR was conducted with SYBR Green Master Mix (Roche Applied Science, Germany). Primer sequences are listed in Table 1.

Table 1
Primers used for RT-PCR analysis.

Gene	Primer direction	Primer sequence
CD80	Forward	5′-AGTTTCTCTTTTTCAGGTTGTGAA -3′
	Reverse	5′-CACCCGGCAGATGCTAAAGA -3′
CD86	Forward	5′-CCACGATGGACCCCAGATG -3′
	Reverse	5′-CCTTTGTAAATGGGCACGGC -3′
CD206	Forward	5′-AGGCTGATTACGAGCAGTGG -3′
	Reverse	5′-CCATCACTCCAGGTGAACCC-3′
Arg-1	Forward	5′-ACATTGGCTTGCGAGACGTA -3′
	Reverse	5′-ATCACCTTGCCAATCCCCAG -3′
ALP	Forward	5′- TCCCAAAGGCTTCTTCTTGC-3′
	Reverse	5′- ATGGCCTCATCCATCTCCAC -3′
OPN	Forward	5′- CCAGCCAAGGACCAACTACA -3′
	Reverse	5′-AGTGTTTGCTGTAATGCGCC -3′
OCN	Forward	5′- TATGGCACCACCGTTTAGGG -3′
	Reverse	5′- CTGTGCCGTCCATACTTTCG-3′
COL-1	Forward	5′-CACGCATGAGCCGAAGCTAA -3′
	Reverse	5′-GGAGGTCCACAAAGCTGAAC -3′
CD31	Forward	5′- CATTACCTGACCAGCGCCA -3′
	Reverse	5′- AGAAACCCGCCCTGTGAAAA -3′
VEGF	Forward	5′- ACGAAAGCGCAAGAAATCCC -3′
	Reverse	5′-CTCCAGGGCATTAGACAGCA -3′
β-Actin	Forward	5′-ACTTTGGGGGATGTTTGCTC -3′
	Reverse	5′-GACTGTTACTGAGCTGCGTTT-3′

2.10. In vitro macrophage polarization with ABOHA @ ZnO hydrogel microspheres

RAW264.7 macrophages were cultured in 12-well plates (1×10^5 cells per well) and treated with lipopolysaccharide (100 ng/ml) for 12 h. The macrophages were then exposed to HAD, AMP, and ABOHA@ZnO hydrogel microspheres for 24 h. After fixation and permeabilization, cells were stained with primary antibodies against CD206, followed by Cy3-conjugated secondary antibodies and DAPI. Images were captured using a confocal microscope. Western blotting was conducted using the methods described above. Membranes were probed with primary antibodies against CD80, CD86, CD206, and Arg-1 overnight at 4 °C, followed by HRP-tagged secondary antibodies. Band images were captured with Scion imaging software. mRNA expression was measured using quantitative reverse transcription–PCR (qRT-PCR) for M1 markers (CD86 and CD80) and M2 markers (Arg-1 and CD206). Primer details and qRT-PCR methods are provided in the supplementary section (Table 1).

2.11. Transcriptome analysis of ABOHA@ZnO-treated BMSCs and RAW264.7

To gain additional insight into the anti-inflammatory, pro-inflammatory, and growth regulator profiles after ABOHA @ ZnO treatment, we examined the gene expression profiles in BMSCs and RAW 264.7 cells. RNA sequencing was performed on the Illumina NovaSeq 6000 at Majorbio, Shanghai. Total RNA from RAW264.7 and BMSCs exposed to Control and ABOHA @ ZnO was extracted using the TRIzol kit and assessed with an Agilent Bioanalyzer and agarose gel electrophoresis. cDNA was purified using the QiaQuick kit, processed, and sequenced. Differentially expressed genes (DEGs) were identified with DESeq2, selecting genes with a p-value <0.05. Principal component analysis was conducted in R to assess sample duplication, and heatmaps were generated for visualization. Gene Ontology (GO) and Kyoto Encyclopedia of Genes and Genomes (KEGG) analyses were performed in R software to identify enriched pathways, with gene set enrichment analysis (GSEA) completing the enrichment analysis.

2.12. In vivo experiments

2.12.1. In vivo skull bone defect model

Sprague Dawley (SD) rats were randomly assigned to four experimental groups (n = 10 each): control, HAD, AMP, and ABOHA@ZnO hydrogel microspheres. Before the surgical procedure, the rats were anesthetized with 2 % pentobarbital sodium administered through intraperitoneal injection. The skull was exposed by making a careful incision on the scalp and performing blunt dissection of the overlying skin. A circular bone defect, 3 mm deep and 5 mm in diameter, was precisely drilled into the cortical bone of the rat skull. The bone defect was then injected with 100 μl MRSA suspension (1×10^6 CFU/ml). After 30 min of bacterial proliferation, the defect area was filled with different materials as per the experimental groups, the wound was sutured, and the rats were returned to their cages for normal post-operative care. Seven d after treatment, skull and cranial soft tissue samples from the regions adjacent to the skull defects were harvested for bacteriological analysis, with bacterial counts primarily determined through RT-PCR by our previous research [26]. After 4 and 8 wks of recovery, the rats were humanely killed through excessive CO_2 inhalation. The skull bones were retrieved for histological and radiological analysis to assess bone regeneration within the bone defect.

2.12.2. H&E, Masson trichrome, and micro-CT analyses

Micro–computed tomography (CT) scanning with a resolution of 8.82 μm was performed to evaluate bone volume, mineral density, and trabecular architecture in the skull defects. At 4 and 8 wks following the implant procedure, the samples were collected and preserved in a 4 % paraformaldehyde solution for 48 h. Regions of interest (ROIs) were identified within the region affected by the surgery, and the bone volume-to-tissue volume ratio (BV/TV) and bone mineral density (BMD) for each specimen were determined from these ROIs. Following micro-CT examination, skull specimens underwent decalcification in a

decalcifying solution at 37 °C, dehydration in a series of increasing alcohol concentrations, embedding in paraffin, and sectioning into 5-micron-thick slices. These sections were stained with hematoxylin and eosin (H&E) and Masson's trichrome to evaluate new bone tissue formation at 4 and 8 wks post-implantation.

2.12.3. IF/IFC staining

SD rat skulls with bone defects were fixed in 4 % paraformaldehyde and dehydrated. After decalcification, paraffin-embedded sections were stained for immunohistochemistry (IHC) with antibodies against osteopontin (OPN), interleukin-10 (IL-10), and tumor necrosis factor-alpha (TNF-α), as well as for immunofluorescence (IF) with antibodies against CD31 and CD163 to assess osteoblast activity, angiogenesis, and anti-inflammatory responses. Images were captured using ImageJ software for quantitative analysis.

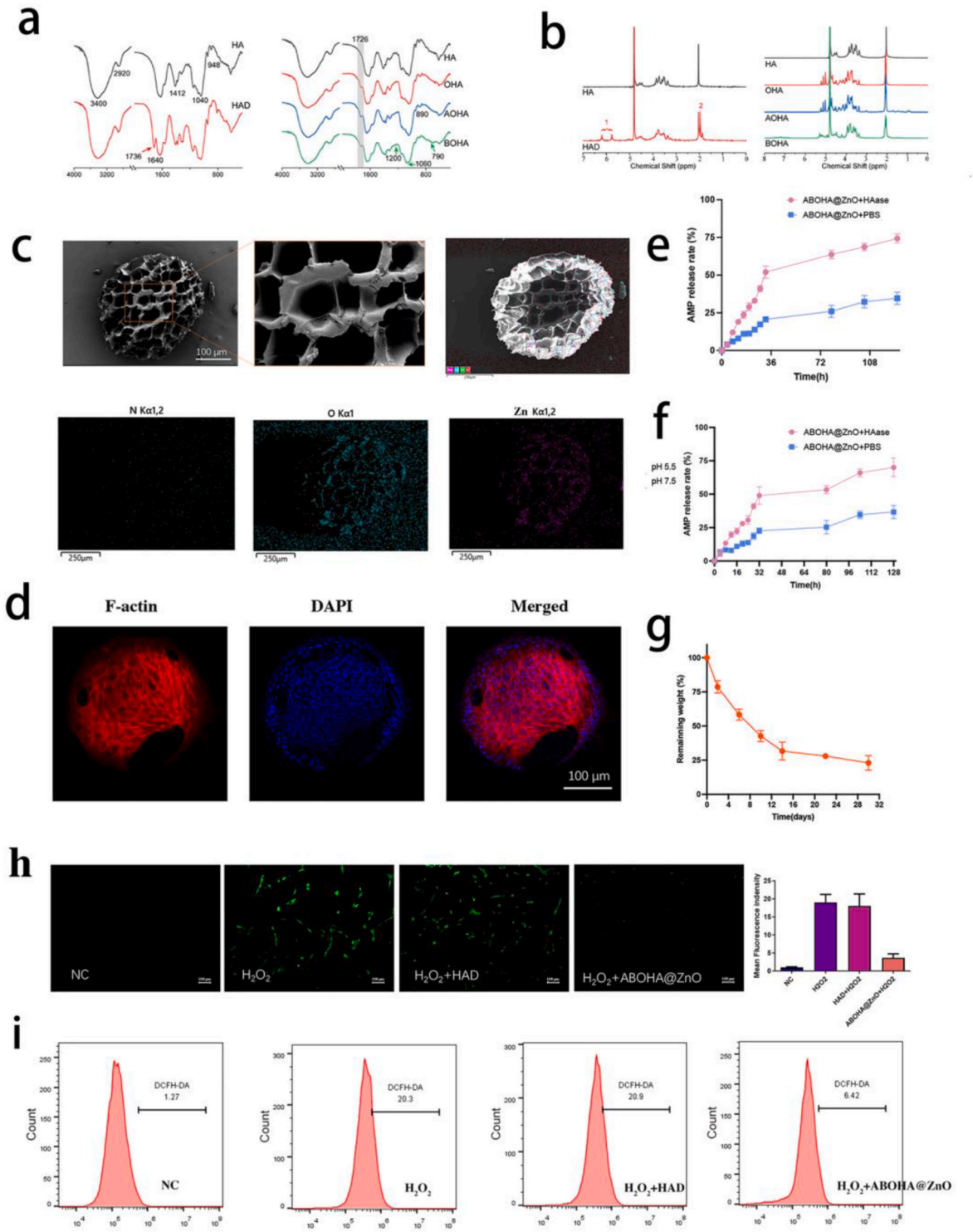

Fig. 1. Characterization of ABOHA@ZnO. (a) FTIR spectra. (b) NMR spectra. (c) Scanning electron microscopy and elemental analysis. (d) Skeleton staining analysis of BMSCs on ABOHA@ZnO sample surfaces for 3 d. (e) AMP release curves from ABOHA@ZnO with HAase or not. (f) AMP release curves from ABOHA@ZnO in pH 5.5 and 7.5. (g) Degradation curve of ABOHA@ZnO. (h–i) ROS scavenging ability of ROS ABOHA@ZnO.

2.12.4. Statistical analysis

All tests were repeated three times with consistent results. Data analysis was performed using SPSS 14.0 software for Windows. Statistical comparisons were made using Student's t-test or two-way analysis of variance (ANOVA) through GraphPad Prism v8 software. Values were considered statistically significant at $p < 0.05$.

3. Results and discussion

3.1. Characterization of ABOHA@ZnO hydrogel microspheres

Infrared spectroscopy of HA revealed characteristic absorption bands: a strong peak at 3400 cm^{-1}, corresponding to O-H stretching vibrations of hydroxyl groups, and a band near 2920 cm^{-1}, indicating -CH_2- group stretching vibrations. The presence of an acetylamino group was confirmed by the band near 1412 cm^{-1}, while bands at 1040 cm^{-1} and 948 cm^{-1} correspond to C-O-C stretching vibrations. The modified derivative, HA derivative (HAD), retained these characteristic HA bands after modification, indicating that the primary structure of HA was preserved. Additionally, HAD exhibited a new peak at 1736 cm^{-1}, characteristic of the carbonyl group (-C=O-) in ester bonds, and a peak at 1640 cm^{-1}, suggesting successful conjugation of methacrylate groups and enabling photopolymerization (Fig. 1a).

Further modifications led to the formation of OHA, AOHA, and BOHA, all of which retained the characteristic HA peaks, confirming structural integrity post-modification. Specifically, the 1726 cm^{-1} peak in the OHA spectrum is attributed to -CHO, indicating successful oxidation and introduction of the reactive -CHO group. In the AOHA spectrum, the peak at 3430 cm^{-1}, shifted to a lower frequency, represents the stretching vibration of aliphatic -NH_2, while the peak at 890 cm^{-1} indicates the bending vibration of -NH_2, suggesting the successful incorporation of AMPs. The BOHA spectrum showed peaks at 1200 cm^{-1} for O-B vibration, 1060 cm^{-1} for O-B-O bending, and 790 cm^{-1} for the benzene ring, indicating successful introduction of boric acid (Fig. 1a).

^{1}H NMR spectroscopy (Fig. 1b), using D_2O as the solvent, was employed to further characterize the structures of HA, HAD, and HADA. The solvent peak of D_2O was observed at δ4.79 ppm, while the region δ3-4 ppm represents the characteristic proton peaks of the sugar ring structure in HA. The peak at δ2.01 ppm is attributed to the methyl hydrogens on the side chain's N-acetylglucosamine. These findings collectively validate the successful modification and structural integrity of HA and its derivatives. To evaluate the external structure of the spatially and temporally controlled hydrogel microspheres, scanning electron microscopy (SEM) and confocal laser scanning microscopy were used (as shown in Fig. 1c and d). The observations confirmed the presence of three-dimensional, spherical, and smooth forms. SEM images further revealed that the exterior of these microspheres had a porous, circular pattern. Elemental analysis by SEM indicated that ZnO NPs were incorporated into the microspheres (the blue dots indicate Zn). F-actin cytoskeleton staining fluorescence images showed that the cells incubated with various samples exhibited well-spread morphology and high viability. The remaining mass of ABOHA@ZnO hydrogel microspheres was observed to decrease progressively over time, at a controlled rate, which is advantageous for the sustained release of pharmaceuticals (Fig. 1g).

3.2. Microspheres exhibit multi-stimuli response and therapeutic effects on infectious bone defects

Under normal conditions, the pH of the human body is neutral, but in the microenvironment of bacterial infections, the pH often becomes acidic [27]. Therefore, designing pH-responsive hydrogels is crucial for treating infectious bone defects, as they can intelligently release drugs in response to the acidic environment of the infected area, effectively inhibit bacterial growth, and promote osteoblast proliferation for infection control and bone defect repair [28]. *S. aureus* secretes hyaluronidase, an enzyme that aids in bacterial dissemination through host tissues [29]. Hyaluronidase promotes bacterial invasion and infection by degrading HA in the extracellular matrix and plays a key role in the pathogenesis of *S. aureus* [30]. This enzyme degrades HA molecules into smaller fragments by hydrolyzing the glycosidic bonds [31]. This study investigated the release of AMPs from the hydrogel microspheres under acidic conditions and in the presence of hyaluronidase. The results showed that hydrogel microspheres released AMP more quickly in specific environments, which is beneficial for drug delivery and tissue engineering, where controlled release and degradation are crucial. The presence of hyaluronidase enhanced AMP release (Fig. 1e), highlighting the hydrogel's sensitivity to enzymatic activity typically found at inflammation or infection sites. Under acidic conditions, the microspheres exhibited a significant AMP release (Fig. 1f) due to the reversible imine bonds in the AOHA hydrogel grafted with antimicrobial peptides, which release the peptides when acidity decreases.

ROS negatively affect infected bone defects primarily through oxidative stress damage to surrounding healthy tissues [32]. Although ROS can contribute to bacterial elimination, it cannot differentiate between bacteria and cells, potentially causing damage to healthy tissues and limiting the therapeutic effectiveness for infectious bone injuries [33]. The phenylboric acid molecules in the BOHA hydrogel can react with ROS, such as hydrogen peroxide, reducing ROS concentration by forming relatively stable compounds and mitigating oxidative damage to cells. In this study, BOHA hydrogel containing phenylboric acid was successfully printed into microspheres. The results indicated that exposure to ROS led to rapid removal by ABOHA@ZnO hydrogel microspheres (Fig. 1i), suggesting these microspheres are suitable for environments with high oxidative stress. Although ZnO-NPs can also produce ROS [34], the amount in the microspheres was controlled within a safe range. The ROS generated was rapidly decomposed by phenylboric acid in the microspheres. ZnO-NPs have shown potential in osteogenesis by releasing zinc ions to activate osteoblasts, promote their proliferation and differentiation, and enhance the extracellular matrix mineralization [35]. Zinc ions can also upregulate the expression of osteogenic genes, thereby promoting bone formation [36]. Additionally, the antimicrobial properties of ZnO-NPs are crucial for controlling infections around bone defect, creating an infection-free environment for bone regeneration [37]. Our study demonstrated that hydrogel microspheres containing ZnO-NPs exhibited significant osteogenic and anti-inflammatory effects, which will be further validated *in vivo* and *in vitro*.

3.3. Antimicrobial properties of ABOHA@ZnO hydrogel microspheres and biocompatibility test

Anti-infection strategies are crucial in treating infectious bone defects [38], a major challenge in orthopedic care. These defects often involve chronic infections caused by bacterial biofilms, which are hard to eliminate [39], thereby increasing patient suffering and complicating the treatment. Applying anti-infection strategies effectively controls infections, reduces bacterial load, prevents the spread of infections, and supports the repair and regeneration of bone tissue. The antibacterial properties of materials used in treating these defects are thus vital. In colony count tests, ABOHA@ZnO hydrogel microspheres significantly reduced *S. aureus* growth after 12 and 24 h compared with both HAD and control groups (Fig. 2a and b, $P < 0.05$), showing enhanced antibacterial effects due to ZnO NPs.

Bacterial biofilms significantly challenge the treatment of infectious bone defects by increasing bacterial resistance and complicating surgeries, leading to higher recurrence rates of infections [40]. The fluorescence imaging results of bacterial biofilms showed that ABOHA@ZnO hydrogel microspheres notably inhibited biofilm formation after 12 and 24 h compared to the HAD, AMP, and control groups (Fig. 2c). Fig. 2d shows the ratio of Live/Dead bacteria in the biofilms of different groups at 12 and 24 h that the antimicrobial effect of the microsphere

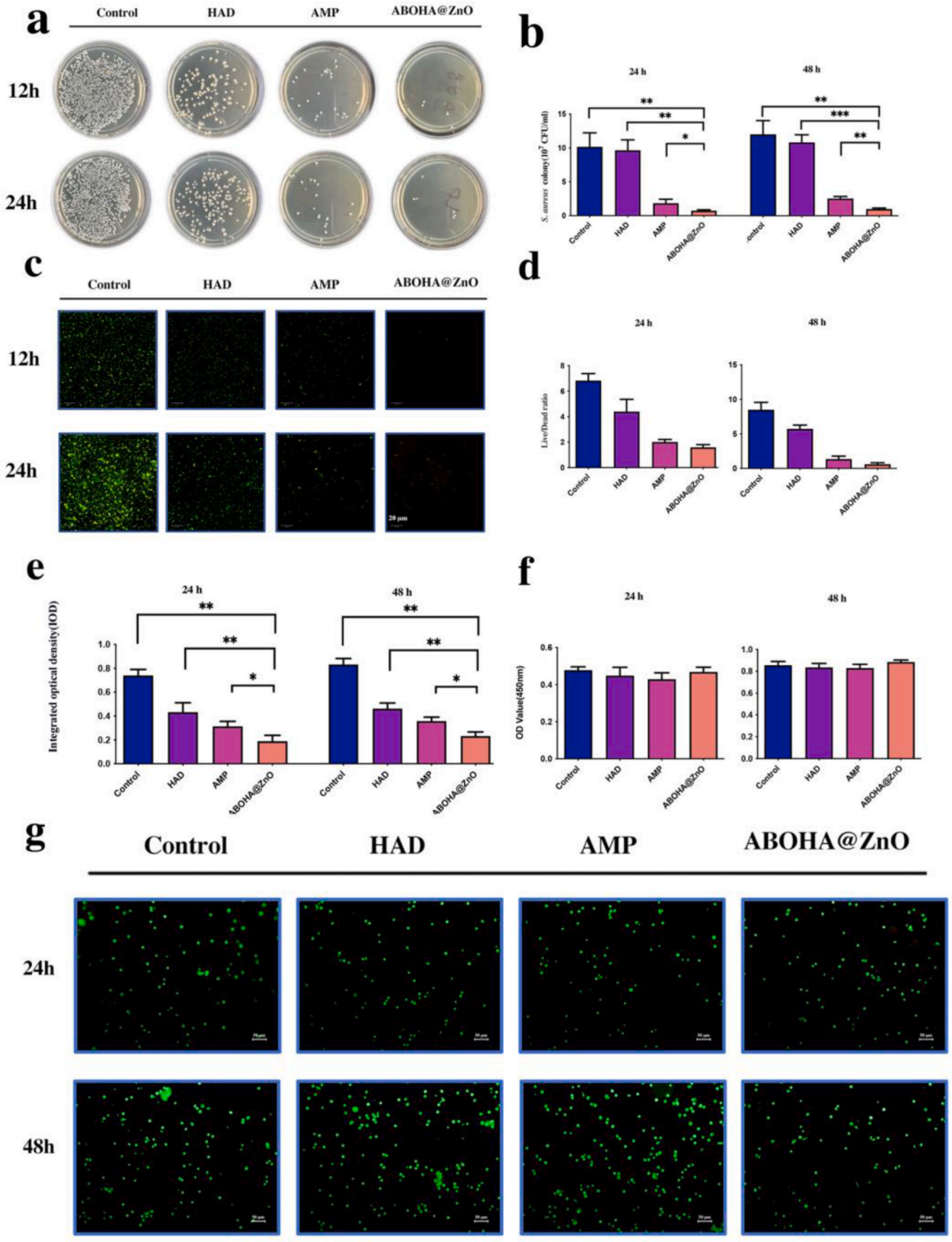

Fig. 2. Antibacterial activity, anti-biofilm effects, and biosafety studies *in vitro* evaluation. (a, b) S. aureus colonies. (b) colony count from different groups for 12 and 24 h. (c) Confocal laser microscopy after live/dead biofilm staining for 12 and 24 h. (d) Live and dead biofilm ratio comparing MRSA treated with ABOHA@ZnO hydrogel microspheres and untreated. (d) Biofilm-integrated optical density (IOD) values. (f) Confocal laser microscopy results after live/dead staining *in vitro* biosafety studies, (h) optical density (OD) value of BMSCs for 24 h and 48 h *$p < 0.05$, **$p < 0.01$, and ***$p < 0.001$.

treatment, which is likely reflected by a higher proportion of dead bacteria, indicating that the treatment significantly reduces the number of viable *S. aureus* within the biofilm. The quantitative analysis of bacterial biofilm using IOD shows that the ABOHA@ZnO group significantly inhibited the growth of *S. aureus* biofilm at both 12 and 24 h (Fig. 2e, $P < 0.05$). These results demonstrate that ABOHA@ZnO hydrogel microspheres effectively reduce the viability and growth of *S. aureus* biofilms, suggesting their potential as an effective antimicrobial agent. The enhanced biofilm inhibition observed with the ABOHA@ZnO group highlights the synergistic effects of ZnO NPs and AMPs,

which could be beneficial for infection control in biomedical applications.

The biocompatibility of hydrogel microspheres is critical for their use in bone defect repair. *In vitro* cytotoxicity assays using bone marrow stem cells (BMSCs)—crucial for bone healing—showed that the microspheres did not negatively impact cell viability or proliferation. After 24 and 48 h of exposure, the survival and growth rates of BMSCs treated with ABOHA@ZnO hydrogel microspheres were comparable to other groups, suggesting no systemic toxicity and confirming their safety for treating bone defects (Fig. 2f and g). Their biocompatibility underscores their potential in regenerative bone medicine.

3.4. Immunomodulatory and osteogenic properties of ABOHA@ZnO hydrogel microspheres on BMSCs

ZnO-NPs exhibit significant osteogenic activity due to their unique physical and chemical properties [35]. ZnO-NPs enhance cell adhesion, spreading, proliferation, osteogenic differentiation, and mineralization both *in vitro* and *in vivo* [41]. This section details experiments designed to explore the molecular mechanisms and bone formation capacity of these hydrogel microspheres, organized into several groups: control, 0.5 % HAD hydrogel extract, 0.5 % AMP, and 0.5 % ABOHA@ZnO hydrogel microspheres extract. Initial findings from IF (Fig. 3a) assays and confocal fluorescence microscopy show elevated signals for OPN and OCN in the ABOHA@ZnO hydrogel microspheres groups (Fig. 3a–c).

To further assess the osteogenic ability of the ZnO-NPs hydrogel microspheres, BMSCs were seeded with extract solutions from the hydrogel microspheres and subjected to staining with ALP and alizarin red (ARS) on day 7, under osteogenic conditioned medium (Fig. 3d and e). ALP staining revealed that the staining intensity in the ABOHA@ZnO hydrogel microspheres group was significantly higher than in the control, HAD, and AMP groups. The ARS staining, which detects calcium-binding proteins, showed that BMSCs in the ABOHA@ZnO hydrogel microspheres group had the most pronounced calcium deposition.

Specifically, the study focused on evaluating the mRNA levels of several key osteogenic markers in BMSCs on the 7th day of culture (Fig. 3f–k). The markers were as follows: ALP, an early indicator of osteogenic activity; OCN, a late marker of osteoblast activity; OPN, crucial for bone remodeling and inflammation; and Col-1, important for bone matrix and mineralization. Gene expression was analyzed using quantitative real-time PCR to understand their regulation during the osteogenic and angiogenesis processes. RT-PCR findings showed that ABOHA@ZnO hydrogel microspheres specifically induced overexpression of the osteogenic genes OCN, OPN, ALP, and Col-1 in BMSCs compared with the other three groups (Fig. 3e–k). Western blot results were consistent with RT-PCR findings, showing significantly increased expression of osteogenic cytokines OCN, OPN, ALP, and Col-1 in the ABOHA@ZnO hydrogel microspheres group compared with the other three groups (Fig. 3l and m). The role of ABOHA@ZnO hydrogel microspheres in bone formation is achieved by regulating several osteogenic markers. ALP (alkaline phosphatase) promotes bone matrix mineralization, and ABOHA@ZnO hydrogel microspheres accelerate mineral deposition and bone formation by enhancing ALP activity. OCN (osteocalcin) plays a role in the later stages of osteogenesis, with its high expression indicating osteoblast maturation and bone matrix mineralization. ABOHA@ZnO hydrogel microspheres accelerate osteoblast maturation by promoting OCN expression. OPN (osteopontin) is involved in bone remodeling and also regulates immune responses. ABOHA@ZnO hydrogel microspheres may optimize the immune microenvironment and promote bone repair by modulating OPN expression. Furthermore, COL-1 (collagen type I), a major component of the bone matrix, is enhanced by ABOHA@ZnO hydrogel microspheres, which improves bone matrix mineralization and bone repair capacity. ABOHA@ZnO hydrogel microspheres promote bone formation through ROS generation and immune regulation. In summary, ABOHA@ZnO hydrogel microspheres play a key role in osteogenesis and bone repair by regulating osteogenic markers such as ALP, OCN, OPN, and COL-1, showing potential for bone defect repair.

A thorough examination of the full set of RNA transcripts confirmed these results. RNA-seq transcriptome analysis was performed on 6 BMSC samples with and without hydrogel microsphere treatment. A comparative gene expression analysis between the hydrogel microsphere-treated and control groups revealed a significant difference in 316 DEGs, with 86 genes upregulated and 230 downregulated (Fig. 4a). KEGG pathway enrichment analysis indicated that these 316 DEGs were significantly concentrated in 20 KEGG pathways, notably the MAPK and PI3K-Akt pathways (Fig. 4b). The heatmap illustrated that most genes involved in osteogenesis were upregulated (Fig. 4c). Quantitative analysis showed that transcripts per million of BMP2, Alp1, Colla1, Runx2, and Opn3 genes were up-regulated in ABOHA@ZnO hydrogel microsphere–treated BMSCs compared with untreated controls (Fig. 4d, $P < 0.05$), consistent with those of western blot and qRT-PCR *in vitro*.

The PI3K-AKT and MAPK signaling pathways significantly influence the osteoblastic process, regulating bone formation and osteocyte function through various molecular mechanisms [42,43]. Activation of the PI3K-AKT pathway promotes osteoblast proliferation and differentiation, enhances extracellular matrix synthesis, and promotes mineral deposition, which is crucial for osteoblast maturation and function [44]. As the core of the PI3K-AKT pathway, PI3K catalyzes the production of PI(3,4,5)P3, activates Akt, promotes osteoblast proliferation and differentiation, and enhances bone formation [45]. Additionally, Akt activation regulates cell survival signals, prevents apoptosis, and maintains the stability and activity of bone cells [46]. The MAPK signaling pathways, including ERK, MEK, and p38 MAPK, are also involved in osteoblast proliferation, differentiation, and functional regulation [47]. Notably, the ERK pathway facilitates early osteoblast differentiation by activating downstream transcription factors such as Runx2 and Osterix, which enhances the expression of osteoblast-related genes [48]. MEK regulates osteoblast proliferation and maturation by activating ERK [49], while p38 MAPK is more involved in cellular stress response and cytokine production, contributing to bone resorption and inflammation [50]. To explore the effect of extracellular signals on intracellular signaling, we performed enrichment analyses using the KEGG (Fig. 4b). These analyses highlighted the PI3K-Akt and MAPK signaling pathways as particularly active, suggesting their significant role in signaling. GSEA further confirmed the central role of these pathways in the ABOHA@ZnO hydrogel microspheres group (Fig. 4e). To verify the activation of these pathways by microspheres, we examined the effects on phospho-PI3K, Akt, MEK1/2, and ERK1/2 (p-PI3K, p-Akt, p-MEK1/2, and p-ERK1/2) mRNA levels. Western blot analysis revealed significantly higher protein expression of p-Akt, p-MEK1/2, and p-ERK1/2 in the ABOHA@ZnO groups compared with the control groups, indicating that the PI3K-Akt and MAPK pathways can be activated by ABOHA@ZnO hydrogel microspheres (Fig. 4f–h). The PI3K-AKT and MAPK signaling pathways promote osteogenesis through interaction with the cellular microenvironment. After receptor activation, PI3K generates PI(3,4,5)P3, which activates AKT, thereby promoting cell survival, proliferation, and mineralization. In the MAPK pathway, MEK activates ERK, which is involved in regulating the differentiation of osteoblasts and enhances the expression of osteogenic genes through transcription factors such as Runx2. These pathways respond to growth factors, cytokines, and mechanical stimuli, such as BMPs and TGF-β, optimizing the function of osteoblasts. Together, they regulate the cell's response to changes in the microenvironment, enhance osteogenic effects, and are of great significance to bone tissue engineering and regenerative medicine.

3.5. Immunomodulatory and angiogenesis properties of ABOHA@ZnO hydrogel microspheres on HUVECs

HUVECs were cultured with the conductive hydrogel microspheres to assess their ability to stimulate blood vessel formation. The

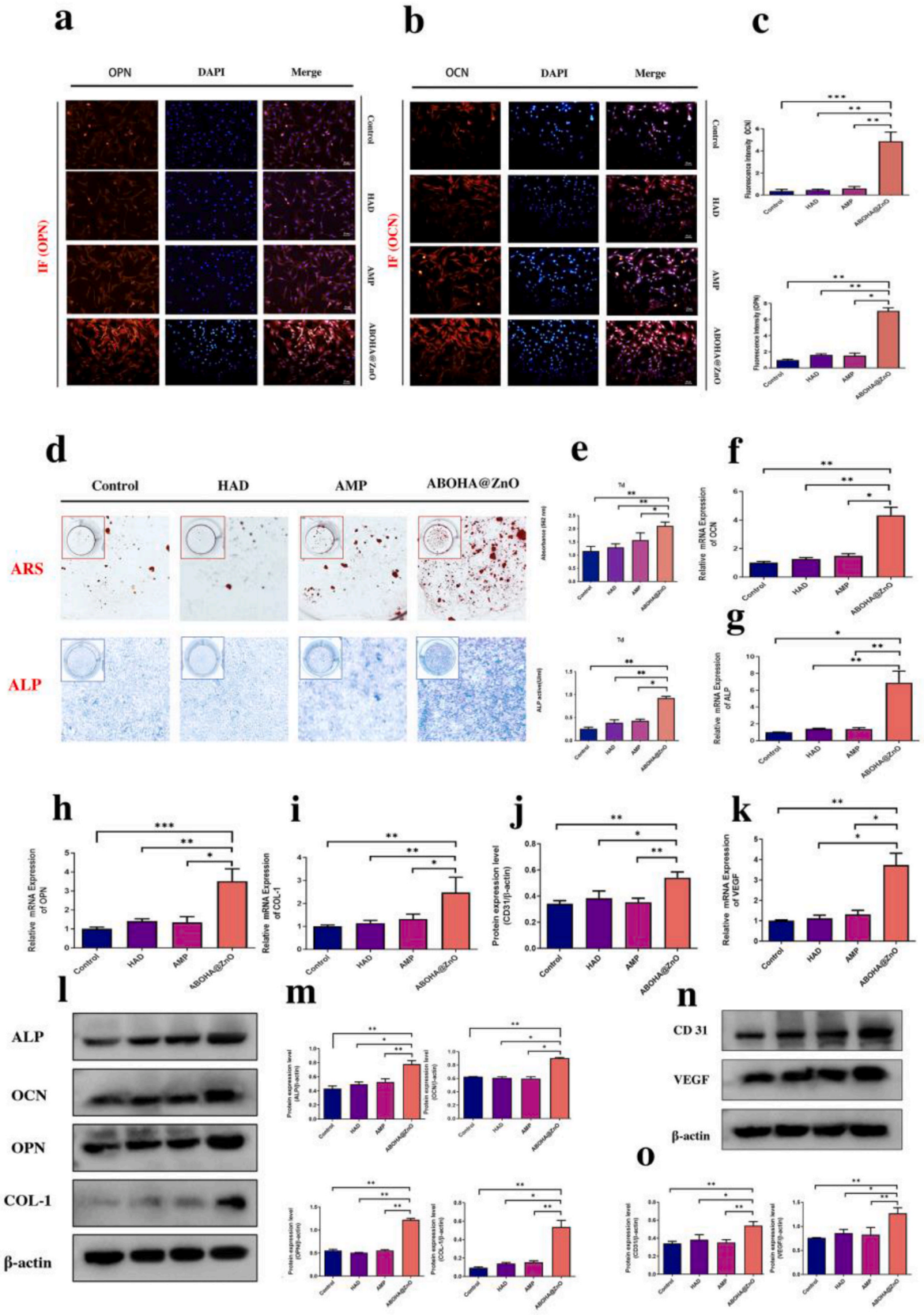

Fig. 3. Effects of osteogenesis and angiogenesis analyses on BMSCs and HUCEs. (a,b) Immunofluorescence staining of OPN and OCN under different conditions. (c) Quantitative analysis of immunofluorescence staining in different groups. (d) Gross and enlarged images of ARS and ALP. (e) Assay results and analysis of ARS and ALP activity in different groups. (f–k) Real-time RT-PCR was performed to determine the gene expression of OCN, OPN, Col-1, ALP, CD31, and VEGF (n = 3). (l–o) Western blot performed to analyze protein expression of OCN, OPN, Col-1, ALP, CD31, and VEGF levels (n = 3). *$p < 0.05$, **$p < 0.01$, and ***$p < 0.001$.

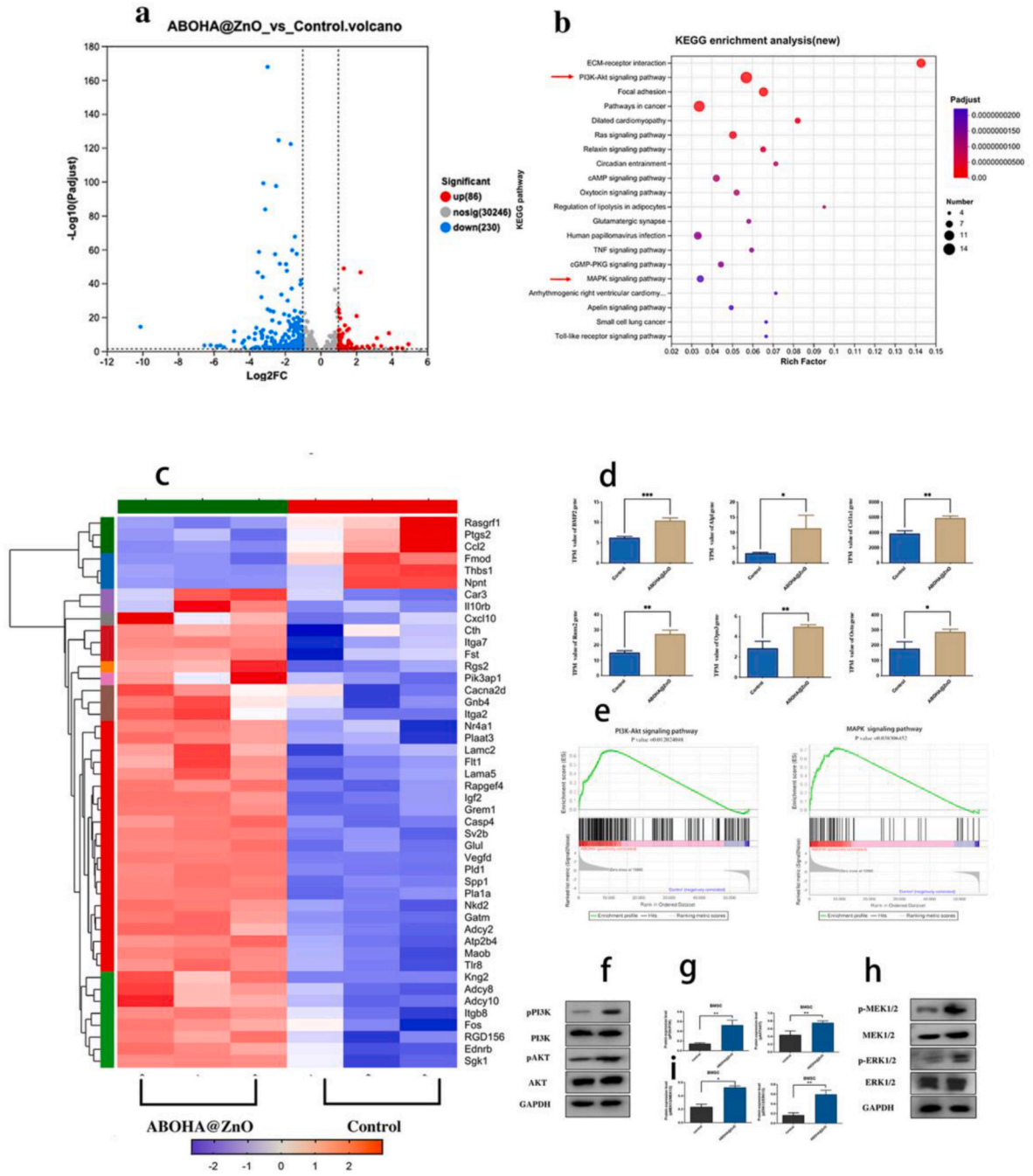

Fig. 4. Transcriptome results of BMSCs treated with ABOHA@ZnO for 48 h. (a) Volcano plot analysis of total DEGs. Red and green dots represent downregulated and upregulated genes, respectively. Gray dots represent genes not statistically significantly different. (b) KEGG enrichment analyses. (c) Heatmap of genes associated with the signal transduction system. (d) Transcripts per million (TPM) of BMP2, Alp1, Colla 1, Runnx2, Opn3, and Ostn. (e) GSEA of PI3K-Akt and MAPK signaling pathway–related features. (f) Western blot performed to analyze PI3K and AKT levels. (g) Quantitative protein level analysis of PI3K and AKT levels. (h) Western blot performed to analyze MEK1/2 and ERK1/2 levels. (i) Quantitative protein level analysis of MEK1/2 and ERK1/2 levels. *$p < 0.05$, **$p < 0.01$, and ***$p < 0.001$. (For interpretation of the references to colour in this figure legend, the reader is referred to the Web version of this article.)

ABOHA@ZnO hydrogel microspheres significantly increased the expression of angiogenesis-related genes, such as CD31 and VEGF (Fig. 3j and k). This was corroborated by higher protein levels of CD31 and VEGF (Fig. 3n and o). CD31, a marker for endothelial cells, is involved in blood vessel formation and maturation, while VEGF is essential for angiogenesis, promoting endothelial cell proliferation and migration, which are crucial for bone repair and regeneration. Therefore, CD31 and VEGF are key in angiogenesis and the coupling of osteogenesis, offering potential targets for enhancing bone regeneration and treating bone healing defects. Our findings suggest that ABOHA@ZnO hydrogel microspheres can increase the expression of vascular-related genes and proteins, thereby promoting angiogenesis.

3.6. Immunomodulatory of ABOHA@ZnO hydrogel microspheres on RAW264.7

Macrophage polarization plays an important role in the treatment of infected bone defects [51]. M1 macrophages, upon activation, release pro-inflammatory cytokines such as TNF-α and IL-1β, which help clear infected and necrotic tissue in the initial stages. However,

overactivation of M1 macrophages may exacerbate tissue damage [52]. By contrast, M2 macrophages are involved in the later stages of inflammation, secreting anti-inflammatory cytokines such as IL-4 and IL-10. These cytokines promote tissue repair and angiogenesis while inducing osteogenic differentiation of bone marrow mesenchymal stem cells, thereby accelerating bone healing [53]. Modulating the physical and chemical properties of biomaterials, or delivering bioactive substances, can guide macrophage polarization from the M1 to the M2 phenotype. This shift optimizes the bone immune microenvironment and promotes bone regeneration. For instance, 3D-printed multifunctional bionic bone scaffolds combined with TP-Mg nanoparticles not only exhibit antibacterial properties but also enhance bone defect repair by promoting M2 macrophage polarization [54]. This strategy offers a new therapeutic approach for infectious bone defects, with the potential to improve treatment outcomes and reduce complications. This study investigated the potential impact of ABOHA@ZnO Hydrogel Microspheres on macrophage immune responses. CD206 markers were selected for immunofluorescent staining to evaluate the immunomodulatory effects on RAW264.7 cells. Immunofluorescence analysis showed a higher intensity of CD206 (M2) in the ABOHA@ZnO hydrogel microspheres group compared with the other three groups (Fig. 5a and b), suggesting that the hydrogel microspheres promoted macrophage polarization from the M1 to the M2 phenotype. Similarly, the AMP group also exhibited higher CD206 intensity, consistent with the results of previous studies [55], and the addition of ZnO NPs enhanced macrophage polarization. To validate the immunofluorescence results,

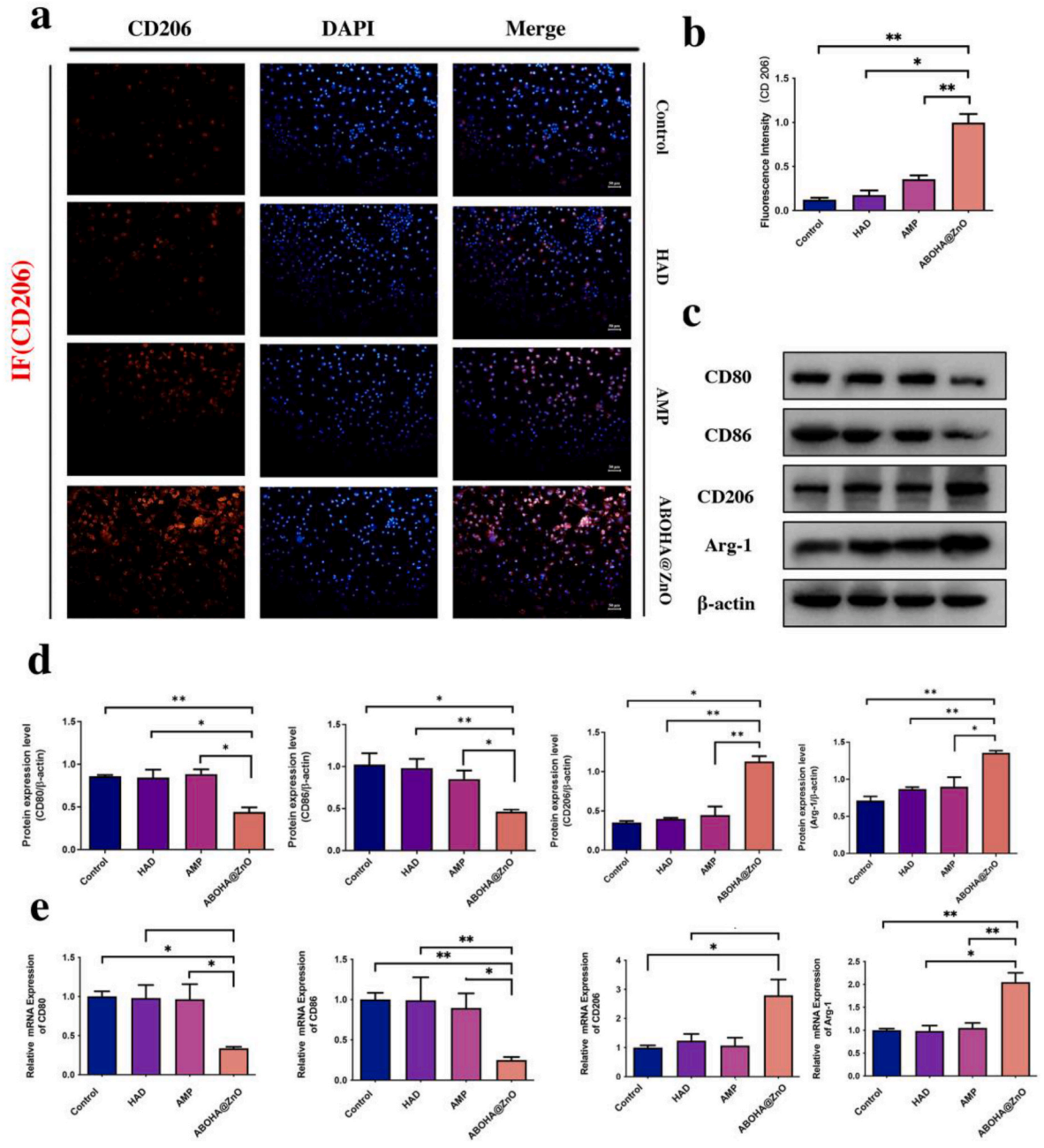

Fig. 5. Effects of macrophage polarization characteristics on RAW264.7. (a) Immunofluorescence staining of CD206 under different conditions. (b) Quantitative analysis of immunofluorescence staining in different groups. (c) Western blots were performed to analyze CD80, CD86, CD206, and Arg-1 levels (n = 3). (d) Quantitative protein level analysis of CD80, CD86, CD206, and Arg-1 levels (e) Real-time RT-PCR was performed to determine the gene expression of CD80, CD86, CD206, and Arg-1 (n = 3). *P < 0.05, **p < 0.01, and ***p < 0.001.

western blot analysis was conducted. Quantitative protein-level analyses indicated that the ABOHA@ZnO hydrogel and AMP groups had higher expression of CD206 and Arg-1 (M2) and lower expression of CD80 and CD86 (M1) than the control and HAD groups. Additionally, the ABOHA@ZnO hydrogel group showed higher expression of CD206 and Arg-1 than the AMP group (Fig. 5c and d), further confirming that the addition of ZnO NPs enhanced macrophage regulation by antimicrobial peptides. RT-PCR results were consistent with the western blot findings, showing that ABOHA@ZnO hydrogel specifically inhibited the expression of CD80 and CD86 (Fig. 5e, $P < 0.05$). Moreover, ABOHA@ZnO hydrogel induced the overexpression of CD206 and Arg-1 compared with the other three groups.

A thorough examination of the full set of RNA transcripts was conducted to confirm previously acquired results. RNA-seq transcriptome analysis was performed on six samples of RAW264.7 cells, both with and without treatment with hydrogel microspheres. A comparative gene expression analysis was conducted between the hydrogel microsphere-treated and control groups. Fig. 6a shows a significant statistical difference in 2935 differentially expressed genes (DEGs), with 1693 genes upregulated and 1242 genes downregulated (Fig. 6a). KEGG pathway enrichment analysis revealed that these 2935 DEGs were significantly concentrated in 20 KEGG pathways, notably the MAPK, PI3K-Akt, and

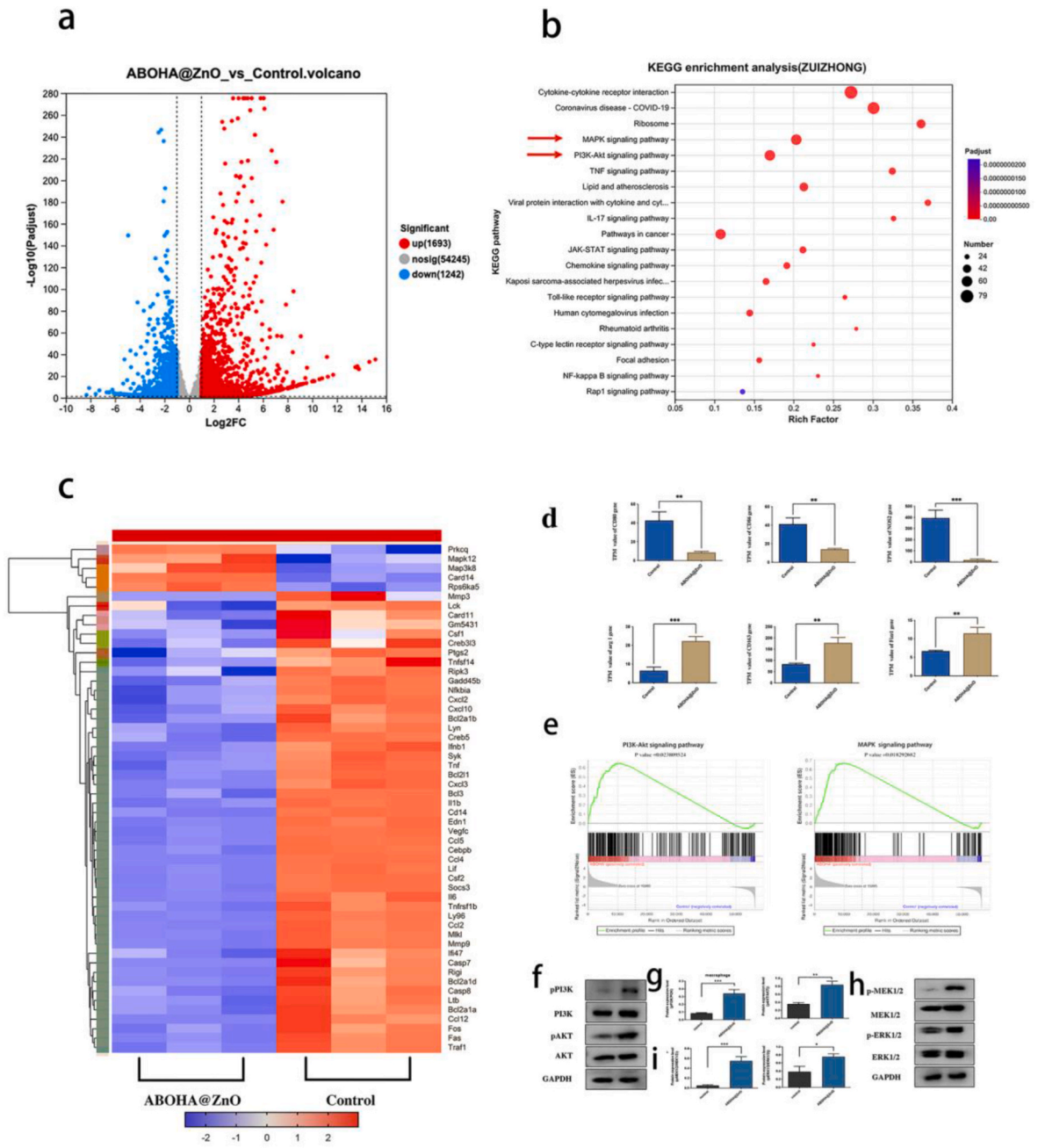

Fig. 6. Transcriptome results of RAW264.7 treated with ABOHA@ZnO for 48 h. (a) Volcano plot analysis of total DEGs. Red and green dots represent downregulated and upregulated genes, respectively. Gray dots denote genes not statistically significantly different. (b) KEGG enrichment analyses. (c) Heatmap of genes associated with the signal transduction system. (d) Transcripts per million (TPM) of CD80, CD86, NOS2, arg1, CD163, and Fizz1. (e) GSEA of PI3K-Akt and MAPK signaling pathway–related features. (f) Western blot performed to analyze PI3K and AKT levels. (g) Quantitative protein level analysis of PI3K and AKT levels. (h) Western blots performed to analyze MEK1/2 and ERK1/2 levels. (i) Quantitative protein level analysis of MEK1/2 and ERK1/2 levels. *$p < 0.05$, **$p < 0.01$, and ***$p < 0.001$. (For interpretation of the references to colour in this figure legend, the reader is referred to the Web version of this article.)

TNF signaling pathways (Fig. 6b). The heatmap illustrated that genes involved in anti-inflammatory responses were mostly upregulated (Fig. 6c). Quantitative analysis of macrophage polarization-related genes showed that, compared with untreated controls, the arg1, CD163, and Fizz1 genes (associated with M2 polarization) were upregulated, while CD80, CD86, and NOS2 were downregulated in ABOHA@ZnO hydrogel microsphere-treated BMSCs (Fig. 6d, $P < 0.05$), consistent with those of western blot and RT-PCR results.

The PI3K-Akt and MAPK signaling pathways play key roles in regulating M2-type macrophage polarization [56]. The PI3K-AKT pathway promotes the activation of mTORC1 and mTORC2 by activating Akt, which enhances the expression of M2-related genes such as arginase-1 (Arg-1) and transferrin, which are crucial for anti-inflammatory responses and tissue repair [57]. Additionally, Akt activation inhibits NF-κB signaling, reducing pro-inflammatory cytokine production and further promoting M2 macrophage polarization [58]. The PI3K gene is also critical in macrophage polarization, affecting cell activation, phenotype, and potentially regulating various biological processes related to inflammation and immune responses [59]. The MEK and ERK genes, as important members of the MAPK signaling pathway, play significant roles in macrophage polarization [59]. MEK facilitates the transmission of intracellular signals by activating ERK, thereby influencing the polarization state of macrophages. During macrophage polarization, activation of the MEK/ERK signaling pathway can promote the polarization of M2-type macrophages [60]. This is achieved by increasing the expression of anti-inflammatory cytokines, such as IL-10, and reducing the production of pro-inflammatory cytokines, such as TNF-α and IL-6. To gain a deeper understanding of how extracellular signals affect intracellular signaling mechanisms, a series of enrichment assessments were conducted using the KEGG for graphical representation (Fig. 6b) on a collection of differentially expressed genes (DEGs). The analyses revealed that the PI3K-Akt and MAPK signaling pathways were particularly active (Fig. 6c–d), suggesting their crucial role in the signaling processes. This finding was further supported by GSEA, which highlighted the critical function of the PI3K-Akt and MAPK pathways in the ABOHA@ZnO hydrogel microspheres (Fig. 6e). To verify the activation of these pathways by hydrogel microspheres, western blot analysis was used to detect the phosphorylation levels of key molecules (PI3K, AKT, MEK1/2, and ERK1/2). The results indicated that the protein expression of p-PI3K/PI3K, p-AKT/AKT, p-MEK1/2/MEK1/2, and p-ERK1/2 was significantly higher in the ABOHA@ZnO hydrogel microspheres groups than in the control group (Fig. 6f–i). These results suggest that hydrogel microspheres can directly activate the AKT, PI3K, ERK, and MEK signals, thereby activating the PI3K-AKT and MAPK pathways. Hydrogel microspheres activate the PI3K-AKT and MAPK signaling pathways through their bioactive components, promoting the polarization of macrophages towards the M2 phenotype. PI3K generates PI(3,4,5)P3 to activate AKT, enhancing the anti-inflammatory and tissue repair functions of M2 macrophages. In the MAPK pathway, MEK activates ERK, which is involved in regulating macrophage polarization and promoting the expression of M2-related genes. These pathways respond to cytokines in the microenvironment, such as IL-4 and IL-10, inducing macrophages to polarize into the M2 phenotype, reducing inflammation, and promoting tissue repair. These results align with *in vitro* cellular experimental outcomes and will be further validated in subsequent animal studies.

3.7. *In vivo optimization of osteogenesis, angiogenesis, anti-inflammatory and acceleration of bone reconstruction*

3.7.1. *Micro-CT imaging evaluation of local bone defects*

Animals were killed at the 4-week and 8-week marks following the implant procedure, with micro-CT scans performed initially to assess mineralized tissue development (Fig. 7a). Given the limited innate healing ability of critical-size bone defects, the blank group showed significantly reduced new bone growth even after 8 wks, indicating the need for further intervention. By contrast, the other three groups exhibited varying degrees of bone formation. Consistent with the *in vitro* findings, the presence of ABOHA@ZnO hydrogel microspheres significantly enhanced bone growth compared to the application of HAD and AMP alone. Additionally, while the application of HAD and AMP led to some results, the healing effects were not as pronounced. HA alone has a certain osteogenic effect. However, combining it with a biological scaffold and adding substances with osteogenic properties can significantly enhance this effect. As the healing period progressed, the ABOHA@ZnO hydrogel microspheres groups showed superior outcomes in bone regeneration, with the highest bone volume-to-tissue volume (BV/TV) ratio and BMD at both 4 and 8 wks (Fig. 7b and c, $P < 0.05$). This study speculates that the early release of antimicrobial peptides is crucial for initiating osteogenic events in bone repair, while the sustained, stepwise release of ZnO NPs initially creates a favorable immuno-microenvironment and later promotes mineralization, supporting ongoing osteogenic processes. Consequently, by the end of the observation period, the ABOHA@ZnO hydrogel microspheres group achieved the most advantageous therapeutic results.

3.7.2. *In vivo antibacterial activity*

Fig. S3 shows the bacterial quantity of MRSA in different treatment groups: Control, HAD, AMP, and ABOHA@ZnO. The ABOHA@ZnO group exhibited a significantly lower bacterial load compared to the Control, HAD, and AMP groups ($p < 0.05$). Notably, the AMP group also showed a reduction in bacterial quantity, though it was less pronounced than the ABOHA@ZnO group. The results indicate that the ABOHA@ZnO hydrogel microspheres significantly reduced MRSA quantity, suggesting their effective antimicrobial properties. The AMP treatment also demonstrated antibacterial activity, though ABOHA@ZnO showed superior efficacy, likely due to the combined antibacterial effects of ZnO and AMP.

3.7.3. *H&E, Masson's trichrome staining, IF, and IHC for histological evaluation*

To further investigate the osteogenic impact of hydrogel microspheres *in vivo*, tissues were stained with H&E and Masson's trichrome staining (Fig. 7d and e). The blank group showed only a small amount of immature bone. By contrast, the control group exhibited compact fibrous tissue due to limited bone formation capacity. When AMP and ZnO NPs were incorporated, the microspheres demonstrated an enhanced capacity for bone formation, leading to the development of new bone tissue.

Intense inflammatory responses can impede bone formation, potentially delaying bone repair or causing implant integration failure [61]. Therefore, the *in vivo* osteogenesis and immunomodulatory capabilities of ABOHA@ZnO hydrogel microspheres were evaluated using immunohistochemical staining for OPN, IL-10, and TNF-α. As shown in Fig. 8a, b, and c, OPN and IL-10 expression levels in the ABOHA@ZnO hydrogel microspheres groups were significantly higher than those in the HAD, AMP, and control groups, with the lowest TNF-α expression levels. These results align with the *in vitro* osteogenesis and anti-inflammatory capacities shown in Fig. 3a and 5a. Bone defect healing requires a synergistic interaction between angiogenesis and osteogenesis. Thus, the efficacy of bone tissue regeneration is closely related to the extent of vascularization achieved. To assess the impact of our microspheres on new blood vessel formation, immunofluorescence analysis for CD31 was performed. The ABOHA@ZnO hydrogel microspheres group showed a significant increase in CD31-positive cells at the defect site, with a remarkable 2–4 times enhancement in blood vessel count compared with the control, HAD, and AMP groups at both 4 and 8 wks postoperatively (Fig. 9a–c). To verify the effect of macrophage regulation in ABOHA@ZnO hydrogel microspheres, we conducted an immunofluorescence (IF) analysis of CD163 (a marker for the M2 phenotype) at 4 and 8 wks. The IF results supported our hypotheses, showing that the ABOHA@ZnO hydrogel microspheres groups had

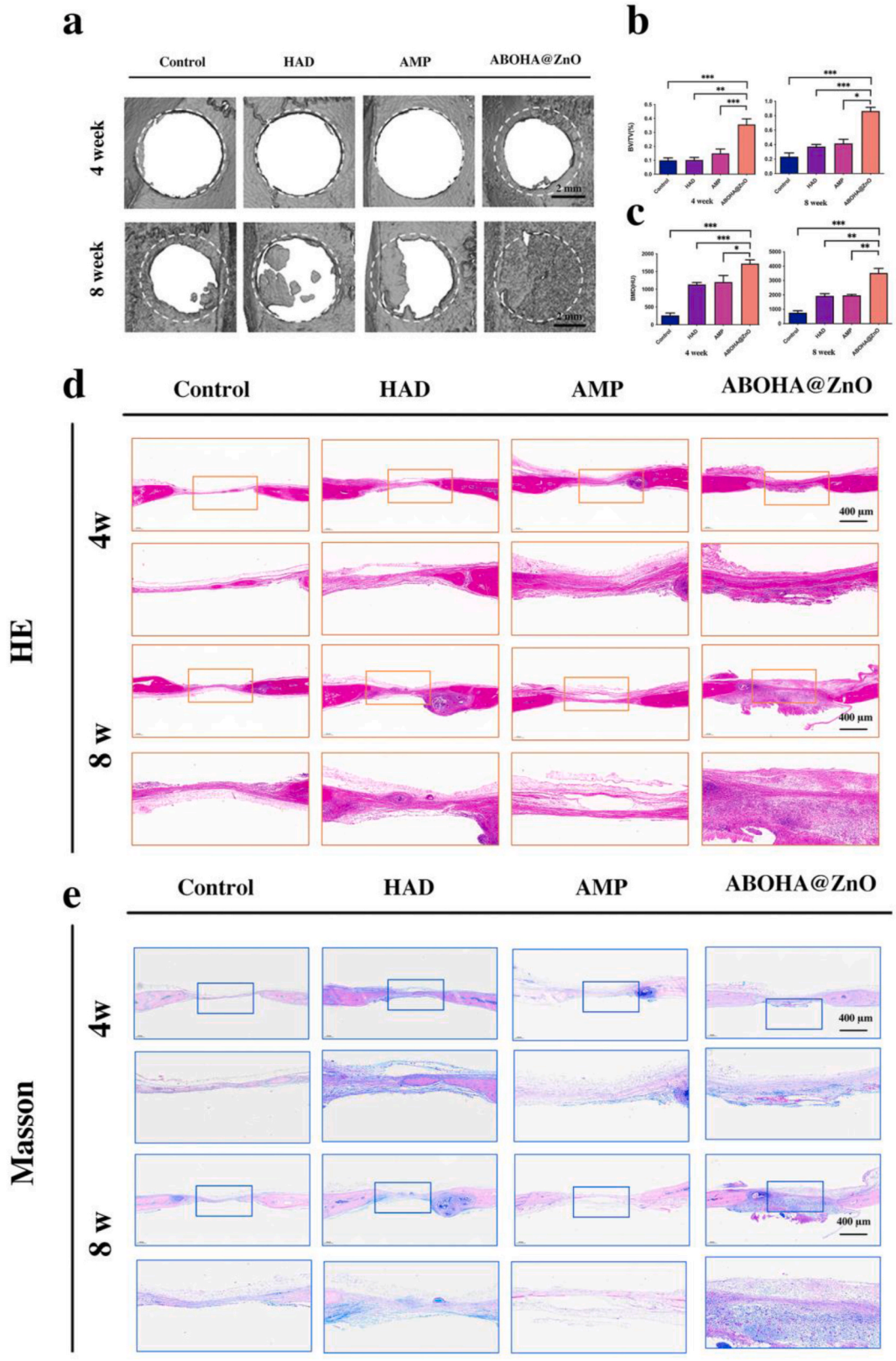

Fig. 7. Morphological assessment and histological analysis of bone defects. (a) Micro-CT reconstruction images captured at 4 and 8 wks post-surgery with the regional magnification of the defect area. (b,c) Quantitative and statistical analysis of BV/TV and BMD (HU). (d,e) Full section images of H&E and Masson's trichrome staining of the skull at 4 and 8 wks post-surgery. *$p < 0.05$, **$p < 0.01$, and ***$p < 0.001$.

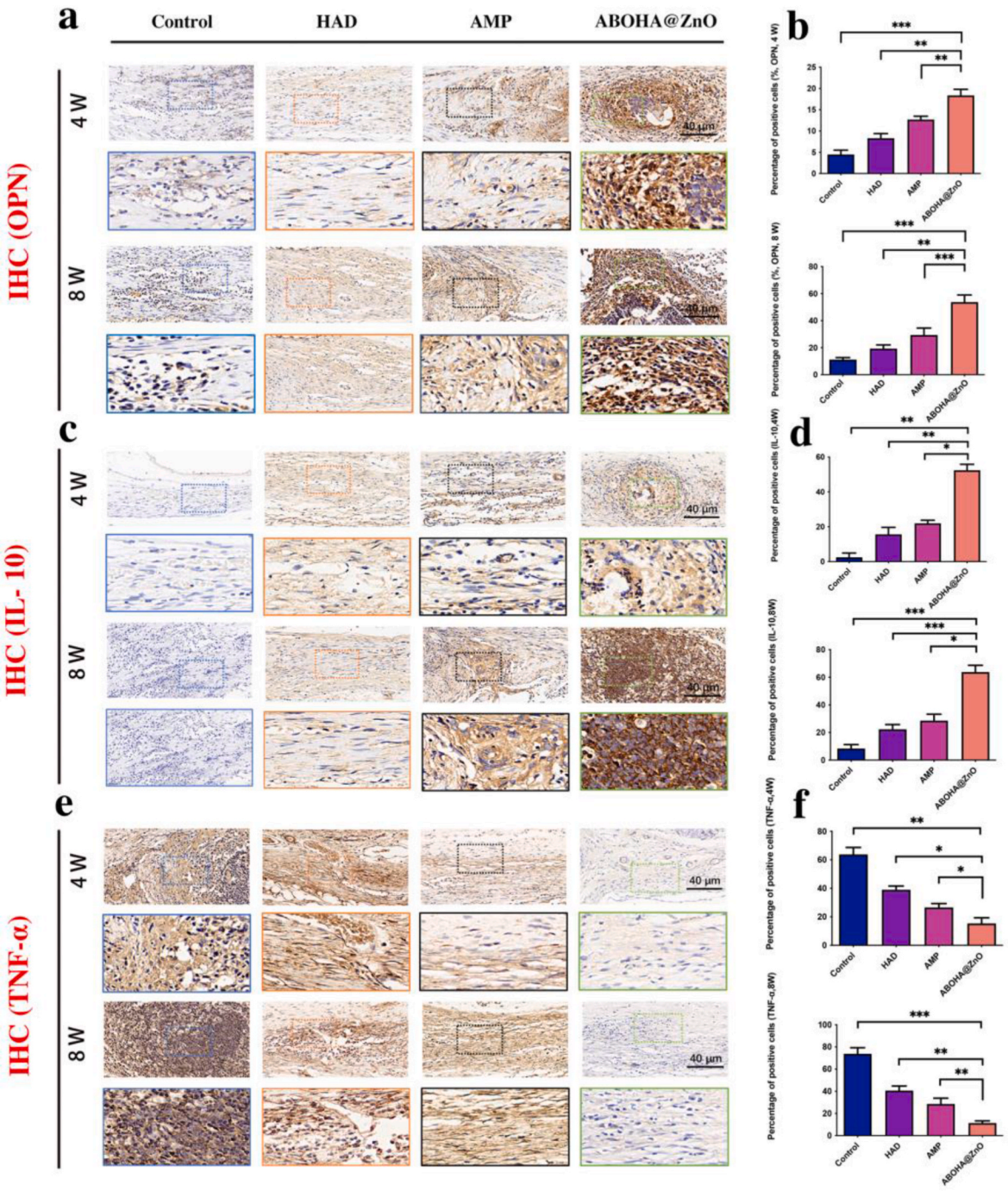

Fig. 8. Anti-inflammatory and osteogenic properties and osteogenesis. (a) Immunohistochemical staining images of osteopontin (OPN) at 4 and 8 wks post-surgery. (b) Semi-quantitative summary of OPN protein expression at 4 and 8 wks post-surgery. (c) Immunohistochemical staining images of IL-10 at 4 and 8 wks post-surgery. (d) Semi-quantitative summary of OPN protein expression at 4 and 8 wks post-surgery. (e) Immunohistochemical staining images of TNF-α at 4 and 8 wks post-surgery. (f) Semi-quantitative summary of OPN protein expression at 4 and 8 wks post-surgery. *$p < 0.05$, **$p < 0.01$, and ***$p < 0.001$.

significantly higher CD163 expression compared with the control, HAD, and AMP groups, as illustrated in Fig. 9d–f. These results were consistent with those from immunohistochemistry, further confirming the effect of the *in vitro* hydrogel microspheres on macrophage polarization to the M2 type.

4. Conclusions

This study introduces a novel 3D-printed HA microsphere hydrogel for treating infectious bone defects. The hydrogel is pH-sensitive, responsive to hyaluronidase, and capable of scavenging ROS. It leverages HA's biocompatibility and biodegradability, with the microsphere structure enhancing cell adhesion, growth, and drug release. The hydrogel microspheres have significant therapeutic effects, releasing antimicrobial peptides in response to the bone defect microenvironment and antioxidants to reduce inflammation-induced oxidative stress, thereby promoting bone repair. The system enables localized treatment of bone defects through direct injection and sustains modulation of the local immune microenvironment over an extended period through a controlled release mechanism. It targets macrophages and influences

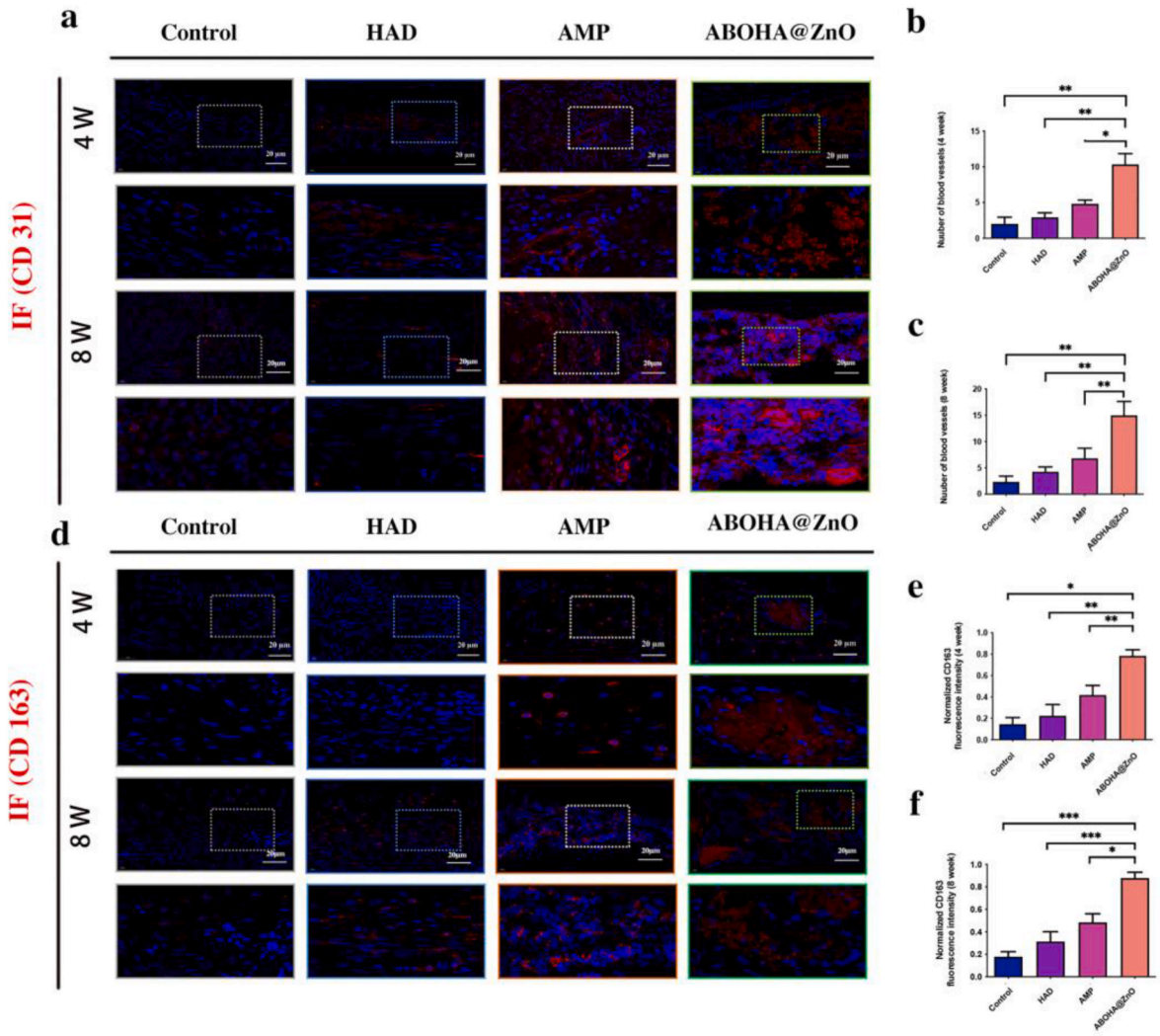

Fig. 9. (a) Immunofluorescence staining images of CD31 at 4 and 8 wks post-surgery. (b,c) Number of blood vessels in different groups at 4 and 8 wks post-surgery. (d) Immunofluorescence staining images of CD163 at 4 and 8 wks post-surgery. (e,f) Semi-quantitative summary of CD163 protein expression at 4 and 8 wks post-surgery. $*p < 0.05$, $**p < 0.01$, and $***p < 0.001$.

BMSCs through activation of the PI3K-AKT and MAPK signaling pathways. These changes in macrophage phenotype and BMSCs, along with the physiological responses during the healing process, contribute to bone regeneration and repair. The microsphere hydrogel's *in vitro* and *in vivo* performance demonstrates its performance as an antibacterial smart hydrogel microsphere and a multi-pathway activator, possessing the function of immune microenvironment regulation with diagnostic and therapeutic capabilities through AMP and ZnO NPs and provides new insights for the treatment of infectious bone defects.

CRediT authorship contribution statement

Xiaolong Lin: Writing – review & editing, Writing – original draft. **Shuli Deng:** Writing – review & editing, Writing – original draft. **Tao Fu:** Writing – review & editing, Writing – original draft. **Yuqing Lei:** Project administration, Methodology, Investigation. **Ying Wang:** Project administration, Methodology, Investigation. **Jiapei Yao:** Formal analysis, Data curation, Conceptualization. **Yaojun Lu:** Formal analysis, Data curation, Conceptualization. **Yong Huang:** Formal analysis, Data curation, Conceptualization. **Jingjing Shang:** Project administration, Methodology, Investigation. **Jingjing Chen:** Software, Resources, Funding acquisition. **Xindie Zhou:** Software, Resources, Funding acquisition.

Consent for publication

All authors approved the final manuscript and the submission to this journal.

Ethics approval

All the animal experiments were approved by the Zhejiang University Institutional Animal Care and Use Committee (No.30013) and conducted ethically according to the principles of the National Research Council's Guide for the Care and Use of Laboratory.

Data availability

All data needed to support the conclusions are present in the paper and/or the Supporting Information. Additional data related to this study are available from the corresponding authors upon reasonable.

Funding

This study was supported by the Key Research and Development Program of Zhejiang under Grant 2022C03060, China Postdoctoral Science Foundation (2024M750277), Science and Technology Project of

Changzhou Health Commission (ZD202319, ZD202339 and QN202356), Basic Research Project of Changzhou Medical Center of Nanjing Medical University (CMC2024PY09), Top Talent of Changzhou "The 14th Five-Year Plan" High-Level Health Talents Training Project (2022CZBJ059, 2022CZBJ060 and 2022CZBJ061), Qinghai Province Health System Guidance Plan Project (2022-wjzdx-106 and 2023-wjzdx-104), and Changzhou Sci&Tech Program(CZ20240029).

Declaration of competing interest

The authors declare that they have no known competing financial interests or personal relationships that could have appeared to influence the work reported in this paper.

Acknowledgements

None.

Appendix A. Supplementary data

Supplementary data to this article can be found online at https://doi.org/10.1016/j.mtbio.2025.101676.

Data availability

All data needed to support the conclusions are present in the paper and/or the Supporting Information. Additional data related to this study are available from the corresponding authors upon reasonable.

References

[1] X. Qiu, et al., Experimental study of β-TCP scaffold loaded with VAN/PLGA microspheres in the treatment of infectious bone defects, Colloids Surf. B Biointerfaces 213 (2022) 112424.
[2] N. Amiryaghoubi, M. Fathi, J. Barar, Y. Omidi, Hydrogel-based scaffolds for bone and cartilage tissue engineering and regeneration, React. Funct. Polym. 177 (2022) 105313.
[3] G. Chakrapani, M. Zare, S. Ramakrishna, Intelligent hydrogels and their biomedical applications, Mater. Adv. 3 (2022) 7757–7772.
[4] A. Di Mola, M.R. Landi, A. Massa, U. D'Amora, V. Guarino, Hyaluronic acid in biomedical fields: new trends from chemistry to biomaterial applications, Int. J. Mol. Sci. 23 (2022) 14372.
[5] S. Amorim, C.A. Reis, R.L. Reis, R.A. Pires, Extracellular matrix mimics using hyaluronan-based biomaterials, Trends Biotechnol. 39 (2021) 90–104.
[6] S. Trombino, C. Servidio, F. Curcio, R. Cassano, Strategies for hyaluronic acid-based hydrogel design in drug delivery, Pharmaceutics 11 (2019) 407.
[7] J. Chen, Y. Su, J. Huo, Q. Zhou, P. Li, Bacteria-responsive hydrogel for on-demand release of antimicrobial peptides that prevent superbug infections and promote wound healing, Colloid Interf. Sci. Commun. 57 (2023) 100752.
[8] V. Silva, et al., Therapeutic potential of dalbavancin in a rat model of methicillin-resistant Staphylococcus aureus (MRSA)-osteomyelitis, Int. J. Antimicrob. Agents 56 (2020) 106021.
[9] V. Silva, et al., Anti-biofilm activity of dalbavancin against methicillin-resistant Staphylococcus aureus (MRSA) isolated from human bone infection, J. Chemother. 33 (2021) 469–475.
[10] Q. Zhou, et al., Fluoroamphiphilic polymers exterminate multidrug-resistant Gram-negative ESKAPE pathogens while attenuating drug resistance, Sci. Adv. 10 (2024) eadp6604.
[11] L. Yu, et al., Antimicrobial peptides and macromolecules for combating microbial infections: from agents to interfaces, ACS Appl. Bio Mater. 5 (2022) 366–393.
[12] H. Mirzaei, M. Darroudi, Zinc oxide nanoparticles: biological synthesis and biomedical applications, Ceram. Int. 43 (2017) 907–914.
[13] A. Sirelkhatim, et al., Review on zinc oxide nanoparticles: antibacterial activity and toxicity mechanism, Nano-Micro Lett. 7 (2015) 219–242.
[14] N. Wang, J.Y.H. Fuh, S.T. Dheen, A. Senthil Kumar, Functions and applications of metallic and metallic oxide nanoparticles in orthopedic implants and scaffolds, J. Biomed. Mater. Res. B Appl. Biomater. 109 (2021) 160–179.
[15] Q. Zhou, et al., Enzyme-triggered smart antimicrobial drug release systems against bacterial infections, J. Contr. Release 352 (2022) 507–526.
[16] Y. Zhang, et al., A zinc oxide nanowire-modified mineralized collagen scaffold promotes infectious bone regeneration, Small 20 (2024) 2309230.
[17] G.C. Ingavle, et al., Injectable mineralized microsphere-loaded composite hydrogels for bone repair in a sheep bone defect model, Biomaterials 197 (2019) 119–128.
[18] S. Zhang, et al., Microsphere-containing hydrogel scaffolds for tissue engineering, Chem.–Asian J. 17 (2022) e202200630.
[19] C. Liu, N. Xu, Q. Zong, J. Yu, P. Zhang, Hydrogel prepared by 3D printing technology and its applications in the medical field, Colloid Interf. Sci. Commun. 44 (2021) 100498.
[20] Q. Gao, J.-S. Lee, B.S. Kim, G. Gao, Three-dimensional printing of smart constructs using stimuli-responsive biomaterials: a future direction of precision medicine, Int. J. Bioprinting 9 (2023).
[21] T. Gai, et al., Engineered hydrogel microspheres for spheroids and organoids construction, Chem. Eng. J. (2024) 155131.
[22] X. Xue, Y. Hu, Y. Deng, J. Su, Recent advances in design of functional biocompatible hydrogels for bone tissue engineering, Adv. Funct. Mater. 31 (2021) 2009432.
[23] Z. Zhao, et al., Injectable microfluidic hydrogel microspheres for cell and drug delivery, Adv. Funct. Mater. 31 (2021) 2103339.
[24] M.B. Asparuhova, V. Chappuis, A. Stähli, D. Buser, A. Sculean, Role of hyaluronan in regulating self-renewal and osteogenic differentiation of mesenchymal stromal cells and pre-osteoblasts, Clin. Oral Invest. 24 (2020) 3923–3937.
[25] N. Ramesh, S.C. Moratti, G.J. Dias, Hydroxyapatite–polymer biocomposites for bone regeneration: a review of current trends, J. Biomed. Mater. Res. B Appl. Biomater. 106 (2018) 2046–2057.
[26] X. Lin, et al., Evaluation of the antibacterial effects and mechanism of Plantaricin 149 from Lactobacillus plantarum NRIC 149 on the peri-implantitis pathogens, Sci. Rep. 11 (2021) 21022.
[27] F. Rippke, E. Berardesca, T.M. Weber, pH and microbial infections, pH Skin: Issues Chall. 54 (2018) 87–94.
[28] K. Lavanya, S.V. Chandran, K. Balagangadharan, N. Selvamurugan, Temperature- and pH-responsive chitosan-based injectable hydrogels for bone tissue engineering, Mater. Sci. Eng. C 111 (2020) 110862.
[29] C.B. Ibberson, et al., Staphylococcus aureus hyaluronidase is a CodY-regulated virulence factor, Infect. Immun. 82 (2014) 4253–4264.
[30] K. Tam, V.J. Torres, Staphylococcus aureus secreted toxins and extracellular enzymes, Microbiol. Spectr. 7 (2019), https://doi.org/10.1128/microbiolspec.gpp1123-0039-2018.
[31] B.A. Buhren, et al., Hyaluronidase: from clinical applications to molecular and cellular mechanisms, Eur. J. Med. Res. 21 (2016) 1–7.
[32] S.K. Bardaweel, et al., Reactive oxygen species: the dual role in physiological and pathological conditions of the human body, Eurasian J. Med. 50 (2018) 193.
[33] C.N. Paiva, M.T. Bozza, Are reactive oxygen species always detrimental to pathogens? Antioxidants Redox Signal. 20 (2014) 1000–1037.
[34] A. Lipovsky, Y. Nitzan, A. Gedanken, R. Lubart, Antifungal activity of ZnO nanoparticles—the role of ROS mediated cell injury, Nanotechnology 22 (2011) 105101.
[35] Y. Li, et al., Enhancing ZnO-NP antibacterial and osteogenesis properties in orthopedic applications: a review, Int. J. Nanomed. 6247–6262 (2020).
[36] T. Lu, et al., Enhanced osteogenesis and angiogenesis of calcium phosphate cement incorporated with zinc silicate by synergy effect of zinc and silicon ions, Mater. Sci. Eng. C 131 (2021) 112490.
[37] E.N. Zare, et al., Metal-based nanostructures/PLGA nanocomposites: antimicrobial activity, cytotoxicity, and their biomedical applications, ACS Appl. Mater. Interfaces 12 (2019) 3279–3300.
[38] C.T. Johnson, A.J. García, Scaffold-based anti-infection strategies in bone repair, Ann. Biomed. Eng. 43 (2015) 515–528.
[39] H. Bezstarosti, et al., Management of critical-sized bone defects in the treatment of fracture-related infection: a systematic review and pooled analysis, Arch. Orthop. Trauma Surg. 141 (2021) 1215–1230.
[40] L. Qin, et al., Prospects and challenges for the application of tissue engineering technologies in the treatment of bone infections, Bone Res. 12 (2024) 28.
[41] Y. Yang, et al., Functionalization of Ti substrate with pH-responsive naringin-ZnO nanoparticles for the reconstruction of large bony after osteosarcoma resection, J. Biomed. Mater. Res. 108 (2020) 2190–2205.
[42] W.B. Jing, H. Ji, R. Jiang, J. Wang, Astragaloside positively regulated osteogenic differentiation of pre-osteoblast MC3T3-E1 through PI3K/Akt signaling pathway, J. Orthop. Surg. Res. 16 (2021) 1–10.
[43] E. Rodríguez-Carballo, B. Gámez, F. Ventura, p38 MAPK signaling in osteoblast differentiation, Front. Cell Dev. Biol. 4 (2016) 40.
[44] Y. Dong, et al., MALAT1 promotes the proliferation and metastasis of osteosarcoma cells by activating the PI3K/Akt pathway, Tumor Biol. 36 (2015) 1477–1486.
[45] V. Carricaburu, et al., The phosphatidylinositol (PI)-5-phosphate 4-kinase type II enzyme controls insulin signaling by regulating PI-3, 4, 5-trisphosphate degradation, Proc. Natl. Acad. Sci. USA 100 (2003) 9867–9872.
[46] J. Zhang, X.-H. Yu, Y.-G. Yan, C. Wang, W.-J. Wang, PI3K/Akt signaling in osteosarcoma, Clin. Chim. Acta 444 (2015) 182–192.
[47] Y. Sun, et al., Signaling pathway of MAPK/ERK in cell proliferation, differentiation, migration, senescence and apoptosis, J. Recept. Signal Transduction 35 (2015) 600–604.
[48] D. Zhang, D. Liu, J. Zhang, C. Fong, M. Yang, Gold nanoparticles stimulate differentiation and mineralization of primary osteoblasts through the ERK/MAPK signaling pathway, Mater. Sci. Eng. C 42 (2014) 70–77.
[49] X. Jin, et al., Daidzein stimulates osteogenesis facilitating proliferation, differentiation, and antiapoptosis in human osteoblast-like MG-63 cells via estrogen receptor–dependent MEK/ERK and PI3K/Akt activation, Nutr. Res. 42 (2017) 20–30.
[50] J. Li, et al., MEK/ERK and p38 MAPK regulate chondrogenesis of rat bone marrow mesenchymal stem cells through delicate interaction with TGF-β1/Smads pathway, Cell Prolif. 43 (2010) 333–343.
[51] N.J. Horwood, Macrophage polarization and bone formation: a review, Clin. Rev. Allergy Immunol. 51 (2016) 79–86.

[52] U. Saqib, et al., Phytochemicals as modulators of M1-M2 macrophages in inflammation, Oncotarget 9 (2018) 17937.
[53] N. Wang, H. Liang, K. Zen, Molecular mechanisms that influence the macrophage M1–M2 polarization balance, Front. Immunol. 5 (2014) 614.
[54] X. Hu, et al., 3D printed multifunctional biomimetic bone scaffold combined with tp-Mg nanoparticles for the infectious bone defects repair, Small (2024) 2403681.
[55] J. Dai, et al., Interpenetrating nanofibrillar membrane of self-assembled collagen and antimicrobial peptides for enhanced bone regeneration, Int. J. Biol. Macromol. 267 (2024) 131480.
[56] D. Zhou, et al., Macrophage polarization and function with emphasis on the evolving roles of coordinated regulation of cellular signaling pathways, Cell. Signal. 26 (2014) 192–197.
[57] K. Tsuji-Tamura, M. Ogawa, Inhibition of the PI3K–Akt and mTORC1 signaling pathways promotes the elongation of vascular endothelial cells, J. Cell Sci. 129 (2016) 1165–1178.
[58] F. Meng, L. Liu, P.C. Chin, S.R. D'Mello, Akt is a downstream target of NF-κB, J. Biol. Chem. 277 (2002) 29674–29680.
[59] E. Vergadi, E. Ieronymaki, K. Lyroni, K. Vaporidi, C. Tsatsanis, Akt signaling pathway in macrophage activation and M1/M2 polarization, J. Immunol. 198 (2017) 1006–1014.
[60] Y.D. Shaul, R. Seger, The MEK/ERK cascade: from signaling specificity to diverse functions, Biochim. Biophys. Acta Mol. Cell Res. 1773 (2007) 1213–1226.
[61] J. Kushioka, et al., Bone regeneration in inflammation with aging and cell-based immunomodulatory therapy, Inflamm. Regen. 43 (2023) 29.